Applied Thermal Engineering 235 (2023) 121368

Contents lists available at ScienceDirect

Applied Thermal Engineering

journal homepage: www.elsevier.com/locate/ate

Research Paper

Multivariable optimization of pyramidal compound substrates for cooling of power-electronics in modern hybrid and electric propulsion systems

F. Ghioldi [a,*], J. Hélie [b], F. Piscaglia [a]

[a] Department of Aerospace Science and Technology (DAER), Politecnico di Milano, Italy
[b] Vitesco Technologies, Toulouse, France

ARTICLE INFO

Keywords:
Electronic cooling
Multivariable thermal optimization
Electric motors
Multilayer compound structures
Pyramidal structures
Spreading resistance

ABSTRACT

We present a method for the optimization of the thermal cooling of heat sources mounted on top of layered composites and pyramidal substrates, that are widely used in the power electronics of hybrid-electric propulsion systems. The analytical solution of the Laplace's heat equation is approximated via Fourier expansion series and it is coupled to the Influence Coefficient Method (ICM) to provide a functional of the overall thermal stress to minimize. A multivariable optimization method is derived by coupling the equations for the heat transfer with the Sequential Least-Square Quadratic Programming (SLSQP), or the Bounded Limited-Memory BFGS (L-BFGS-B) algorithm. Code validation is performed against three-dimensional simulations and experimental data available from the literature. It is shown that an optimal component relocation and apportionment of the overall thickness of the multilayer substrate promotes a sensible reduction of the thermal stress.

1. Introduction

The optimization of the thermal layout employed in battery-powe red electric propulsion systems is of key interest in Automotive and Aerospace. This consists of the minimization of the thermal stress to promote an extension of the lifespan of the components, while performance and safety are preserved [1]. In the analysis of microelectronics, discrete heat sources are commonly employed to represent the electronics arrangement, being placed on rectangular plates subjected to convective cooling. Cooling must ensure sufficient thermal dissipation and the optimum working temperature range for the various components. Several numerical strategies have been developed through the years to thermally characterize the layout of microelectronic configurations. Finite Element Analysis (FEA) and Finite Difference (FD) methods are general and can reliably solve the heat transfer problem in complex geometries [2,3]. Analytical models may represent a fast alternative for specific thermal spreading problems [4–6]. In multilayer packs, the analytical solution of the steady-state heat transfer problem can be found, provided that the electronics arrangement is modeled by externally applied heat sources. Starting from this assumption, non-dimensional equations are available in the literature to predict the temperature and heat flux distribution for single-centered components on top of single isotropic layers [7]. Another analysis reported in [8] handles squared components on top of square substrates connected to fin heat promoters. The extension of the methodology to compound substrates with two isotropic layers and eccentric multi-source arrangements is proposed in [9]; the one for multilayer substrates with perfect adhesion or finite conductance at the interface is reported in [2]. Orthotropic effects can also be formally included in the study [4,10,11]. Similarly, formulations for single-layer anisotropic insulated substrates are proposed in [12], for sources and sinks located at both sides of the cooling channel. The general solution for multi-source layouts on top of anisotropic multilayer structures with finite conductance at the layer-to-layer interface is shown in [4], where progressive simplifications allow to recover the orthotropic and isotropic counterpart expressions, together with the peak and average values of temperature at the source plane for each component. The knowledge of the total resistance connected to each component can be derived from these temperature values. In pyramidal structures, uneven layers are mounted one on top of the other; for these configurations, the analytical solutions of the Laplace equation cannot be found and the temperature distribution is not easy to predict [13], especially with thick and low conductive thermal pad layers [14,15]. A method based on the superimposition of three different contributions is presented in [13] to approximate the total component resistance. Cross-effects among the sources can be predicted via the Influence Coefficient Method (ICM) [16].

The natural step forward consists of optimizing such configurations. Examples of optimization procedures based on analytical models are available in the literature for simplified cases with specific footprints [17], or specific relative positions [18]. Optimization via

* Corresponding author.
E-mail address: federico.ghioldi@polimi.it (F. Ghioldi).

https://doi.org/10.1016/j.applthermaleng.2023.121368
Received 18 April 2023; Received in revised form 12 July 2023; Accepted 14 August 2023
Available online 22 August 2023
1359-4311/© 2023 The Author(s). Published by Elsevier Ltd. This is an open access article under the CC BY license (http://creativecommons.org/licenses/by/4.0/).

Nomenclature

Acronyms

L-BFGS-B	Limited-memory BFGS Bound - Algorithm
PC	Pyramidal configuration
SIPD	Same in-plane dimensions
SLSQP	Sequential Least Squares Programming - Algorithm

Greek Symbols

γ	General eigenvalue of the spreading function [–]
λ, δ, β	Eigenvalue of the spreading function [–]
$\mathcal{X}$	Vector of the state variables [–]
$\boldsymbol{\Phi}$	Spreading function [–]
θ	Temperature excess [K]

Roman Symbols

$\bar{h}$	Average convective heat transfer coefficient [W/m^{2}K]
err_θ	Relative error on peak temperature excess [–]
$\boldsymbol{k}$	Thermal conductivity vector of the solid layer [W/mK]
A	Area [m^2]
A_i, B_i	Fourier coefficients [–]
f_{ij}	Influence coefficient factor [K/W]
i, s	Index for component [–]
j, p	Index for layer in the substrate [–]
L	Substrate length [m]
L_c	Component length [m]
m, n	Summation indexes [–]
N	Number of layers [–]
N_c	Number of components [–]
N_v	Number of variables of the state vector [–]
Q	Heat power [W]
q	Heat flux [W/m^2]
R	Resistance [K/W]
T	Temperature [K]
t	Solid layer thickness [m]
W	Substrate width [m]
W_c	Component width [m]
x, y, z	Cartesian coordinates [m]
X_c, Y_c	Heat source centroid coordinates [m]

Superscript

$(\cdot)^0$	Initial condition
$(\cdot)^k$	Iteration

Subscripts

$1D$	One-dimensional
$3D$	Three-dimensional multi-region
amb	Ambient
$anal$	Referred to the analytical model
$base$	Referred to substrate
c	Referred to component
$init$	Initial, relative to the initial condition
ip	In plane
max	Maximum
min	Minimum
N	Last layer
opt	Optimum
pad	Referred to first layer in pyramidal schemes
red	Reduction
ref	Reference
sp	Spreading
t	Total

neural networks is proposed in [19], but the extensive size of the datasets required for training affects the overall computational cost and time. To overcome this limit, the use of adaptive artificial neural networks is presented in [20,21]; nonetheless, when boundary conditions vary, the computational cost of this approach still looks high. Alternative approaches are based on the use of genetic algorithms, that necessitate the tuning of several constants to adequately evolve through generations and optimize the process itself [22]. A coupling between FEA software and analytical objective functions for thermal and mechanical stress minimization is proposed in [23]. In multi-source arrangements, a FEA-based optimization procedure may lead to high computational costs. A simplified optimization procedure based on the manipulation of the isotropic form of the single-layer solutions is shown in [24]. Similarly, the optimization of highly conductive single layer substrates is reported in [25], to reliably predict the optimal layer thickness for high component-to-base surface ratios only. A preliminary step for the concurrent treatment of multiple variables in sequence is provided in [4], where the optimization procedure is applied to find the optimal layer thicknesses only.

1.1. Motivation of this research

Electrified Propulsion offers new possibilities for reducing fuel and energy usage in Automotive and also in Aviation: Unmanned Aerial Systems (UAS), Urban Air Mobility (UAM) platforms and small passenger aircraft are all good candidates for electric and hybrid-electric propulsion architectures. The thermal design and management in electric motors is crucial to preserve the working temperature range for the various components, to control the device peak temperatures, and to ensure performance, safety and durability. The optimal positioning of the heat sources influences the temperature distribution and the heat transfer across the layer substrates. When used with GaN, pyramidal substrates show excellent properties of passive cooling in compact structures at a very limited costs. At the time the paper is written, a procedure based on analytical models for optimal relocation of multi-source electronics and resizing of multilayer pyramidal substrates is missing in the literature.

1.2. Goals and highlights

The analytical model of [4] has been here extended to predict the temperature distribution and the heat transfer in composite pyramidal substrates. The analytical model has been coupled to the Influence Coefficient Method to account for the presence of multiple components, and it has been included into an automatic multivariable optimizer. The optimizer aims at reducing the total resistance of the multi-source arrangement, that is an indicator of the thermal stress of the overall configuration. This is achieved by modifying the shape of the layers and the positioning of the discrete heat sources (electrical components). The method is validated on compound systems with multilayer substrates sharing the same in-plane dimensions (SIPDs) and with pyramidal configurations (PCs); its effectiveness is evaluated through: (a) the reliability of the solution, by a validation against results from experiments and three-dimensional simulations; (b) the speed of calculation.

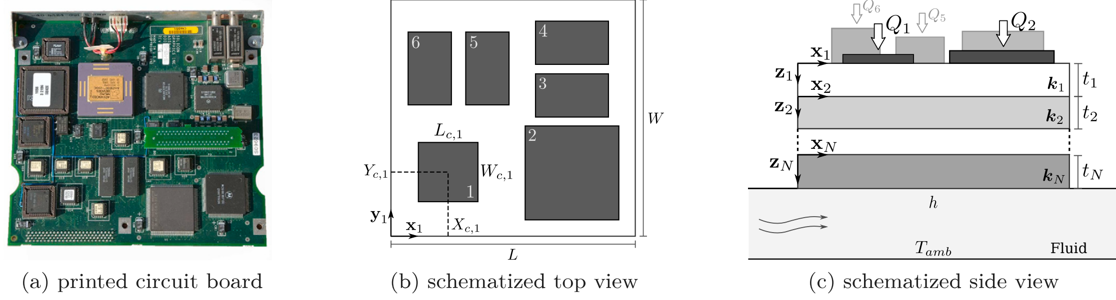

(a) printed circuit board (b) schematized top view (c) schematized side view

Fig. 1. Geometrical description of the electronics mounted on top of a compound substrate.

1.3. Paper structure

The analytical solution to the anisotropic heat transfer equation is presented in Section 2 to predict the temperature distribution in multilayer substrates. The equations are used in Section 3 to calculate the total resistance of the electronics in the case of single- and multi-source configurations. For compound packs with pyramidal structures, a three-term function approximates the total resistance. A validation of the proposed theory is presented in Section 4 on a real power module configuration. Then, the method is included in a multivariable optimizer in Section 5. The validation of the optimizer is proposed in Section 6 on multilayer substrates with same in-plane dimensions, and on pyramidal configurations. A discussion on the rate of convergence to the optimal solution is provided in Section 7, with details on the computational cost of the method. Conclusions are drawn in Section 8.

2. Temperature distribution in multilayer substrates

The typical configuration investigated in this study involves N_c electronic (heat) sources, as shown in Fig. 1. The footprint of the i-th component is $A_{c,i} = L_{c,i} \times W_{c,i}$, and the only source of heat flux q_i from the source is linked to the heat power $Q_i = q_i A_{c,i}$ at the top surface (upper boundary). The electronics is mounted on top of a multilayer anisotropic substrate made of N layers, whose geometrical footprint is $A_{\text{base}} = L \times W$ (Fig. 1(c)). Each layer j is characterized by a thickness t_j and by an anisotropic thermal conductivity $\boldsymbol{k}_j(x, y, z)$.

The temperature distribution in the substrate (Fig. 1) is calculated by the anisotropic steady-state equation for heat conduction:

$$\nabla \cdot (k\nabla T) = k_x \frac{\partial^2 T}{\partial x^2} + k_y \frac{\partial^2 T}{\partial y^2} + k_z \frac{\partial^2 T}{\partial z^2} = 0 \tag{1}$$

The temperature excess with respect to an ambient temperature T_{amb} is defined as:

$$\theta(x, y, z) = T - T_{\text{amb}} \tag{2}$$

Thus, Eq. (1) becomes:

$$k_x \frac{\partial^2 \theta}{\partial x^2} + k_y \frac{\partial^2 \theta}{\partial y^2} + k_z \frac{\partial^2 \theta}{\partial z^2} = 0 \tag{3}$$

The following boundary conditions are applied on the source plane (Fig. 1(b)):

$$\left.\frac{\partial \theta_1}{\partial z}\right|_{z_1=0} = 0 \qquad (x, y) \in (A_{\text{base}} - A_c) \tag{4}$$

$$-k_{z,1} \left.\frac{\partial \theta_1}{\partial z}\right|_{z_1=0} = q \qquad (x, y) \in A_c \tag{5}$$

while for the adiabatic side walls of the structure it holds:

$$\left.\frac{\partial \theta}{\partial x}\right|_{x=0} = \left.\frac{\partial \theta}{\partial x}\right|_{x=L} = \left.\frac{\partial \theta}{\partial y}\right|_{y=0} = \left.\frac{\partial \theta}{\partial y}\right|_{y=W} = 0 \tag{6}$$

For the Nth layer a convective boundary condition states:

$$\left.\frac{\partial \theta_N}{\partial z}\right|_{z_N=t_N} = -\frac{h(x, y)}{k_{z,N}} \theta_N(x, y, t_N) \tag{7}$$

Even though a non-uniform in-plane heat transfer coefficient $h(x, y)$ [26] can be accounted by the optimization process (see Appendix C), a constant average heat transfer coefficient $\bar{h}$ is introduced:

$$h(x, y) \simeq \bar{h} = \frac{1}{A_{\text{base}}} \int_{A_{\text{base}}} h(x, y) dA \tag{8}$$

The solution of Eq. (3) is written in terms of Fourier expansion series after a variable separation:

$$\theta = \sum_{m=1}^{\infty} \sum_{n=1}^{\infty} C(\lambda, \delta) e^{\lambda x} e^{\delta\left(\sqrt{k_x/k_y}\right) y} e^{i\sqrt{\lambda^2+\delta^2}\left(\sqrt{k_x/k_z}\right) z} \tag{9}$$

For anisotropic substrates, the application of Eq. (6) to Eq. (9) produces:

$$\begin{aligned} \theta = {} & A_{00} + B_0 \sqrt{\frac{k_x}{k_z}} z \\ & + \sum_{m=1}^{\infty} \cos(\lambda_m x) \left[A_m \cosh\left(\lambda_m \sqrt{\frac{k_x}{k_z}} z\right) + B_m \sinh\left(\lambda_m \sqrt{\frac{k_x}{k_z}} z\right) \right] \\ & + \sum_{n=1}^{\infty} \cos\left(\delta_n \sqrt{\frac{k_x}{k_y}} y\right) \left[A_n \cosh\left(\delta_n \sqrt{\frac{k_x}{k_z}} z\right) + B_n \sinh\left(\delta_n \sqrt{\frac{k_x}{k_z}} z\right) \right] \\ & + \sum_{m=1}^{\infty} \sum_{n=1}^{\infty} \cos(\lambda_m x) \cos\left(\delta_n \sqrt{\frac{k_x}{k_y}} y\right) \left[A_{mn} \cosh\left(\beta_{mn} \sqrt{\frac{k_x}{k_z}} z\right) \right. \\ & \left. + B_{mn} \sinh\left(\beta_{mn} \sqrt{\frac{k_x}{k_z}} z\right) \right] \end{aligned} \tag{10}$$

for which $\lambda_m = \frac{m\pi}{L}$, $\delta_n = \frac{n\pi}{W}\sqrt{\frac{k_y}{k_x}}$ and $\beta_{mn} = \sqrt{\lambda_m^2 + \delta_n^2}$.

Moreover, by combining Eqs. (7) and (10), it follows:

$$B_0 = -\left(\frac{\bar{h}}{k_{z,N} + \bar{h} t_N}\right) \sqrt{\frac{k_{z,N}}{k_{x,N}}} A_{00} \tag{11}$$

$$B_{i,N} = -\underbrace{\left(\frac{\bar{h} + k_{z,N}\gamma\sqrt{\frac{k_{x,N}}{k_{z,N}}} \tanh\left(\gamma\sqrt{\frac{k_{x,N}}{k_{z,N}}} t_N\right)}{\bar{h} \tanh\left(\gamma\sqrt{\frac{k_{x,N}}{k_{z,N}}} t_N\right) + k_{z,N}\gamma\sqrt{\frac{k_{x,N}}{k_{z,N}}}} \right)}_{\Phi_N(\gamma)} A_{i,N} \tag{12}$$

where γ corresponds to λ_m, δ_n, $\beta_{m,n}$ for $B_i = B_m$, B_n, $B_{m,n}$ respectively, and $\Phi_N(\gamma)$ is the anisotropic spreading function for the bottom layer N. For substrates having a single layer, $\Phi_N(\gamma) = \Phi_1(\gamma)$ (see Fig. 2); for multilayer packs, boundary conditions to model layer-to-layer interface are set to achieve the system closure. Under the assumption of perfect layer-to-layer adhesion, for a layer $j \in [1 : N-1]$ (see Fig. 1(c)) it holds::

$$\theta_j\left(x, y, z = t_j\right) = \theta_{j+1}(x, y, z = 0) \tag{13}$$

$$k_{z,j} \left.\frac{\partial \theta_j}{\partial z}\right|_{z_j=t_j} = k_{z,j+1} \left.\frac{\partial \theta_{j+1}}{\partial z}\right|_{z_{j+1}=0} \tag{14}$$

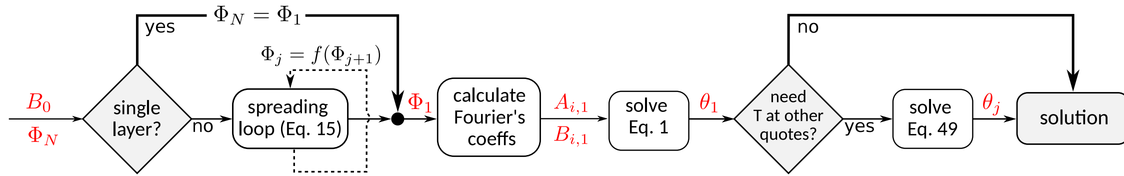

Fig. 2. Procedure to determine the two-dimensional temperature distribution in a multilayer pack.

A different system closure involving finite conductance among the layers is described in [4]. By coupling Eq. (10) with Eqs. (13) and (14), it follows:

$$B_{i,j} = -\underbrace{\left(\frac{\tanh\left(\gamma\sqrt{\frac{k_{x,j}}{k_{z,j}}}t_j\right) + \Phi_{j+1}(\gamma)\sqrt{\frac{k_{z,j+1}}{k_{z,j}}}\sqrt{\frac{k_{x,j+1}}{k_{x,j}}}}{1+\Phi_{j+1}(\gamma)\sqrt{\frac{k_{z,j+1}}{k_{z,j}}}\sqrt{\frac{k_{x,j+1}}{k_{x,j}}}\tanh\left(\gamma\sqrt{\frac{k_{x,j}}{k_{z,j}}}t_j\right)} \right)}_{\Phi_j(\gamma)} A_{i,j} \tag{15}$$

where $\Phi_j(\gamma)$ is the anisotropic spreading function for the layer $j \in [1 : N-1]$. In multilayer substrates, upon the calculation of $\Phi_N(\gamma)$ from Eq. (12), a loop is performed on Eq. (15) to obtain: (a) the values of the spreading function for the remaining upper layers; (b) the temperature distribution at different vertical positions in the pack (see Fig. 2 and Appendix A); (c) the temperature distribution on the heated surface.

From Eq. (5), the anisotropic coefficients A_i are:

$$A_{00} = \frac{Q}{LW}\left(\frac{1}{h} + \sum_{j=1}^{N}\frac{t_j}{k_{z,j}}\right) \tag{16}$$

$$A_m = \sum_{m=1}^{\infty} \frac{4Q\cos(\lambda_m X_c)\sin\left(\lambda_m \frac{L_c}{2}\right)}{LWL_c\ k_{z,j}\lambda_m^2\Phi(\lambda)\sqrt{\frac{k_{x,j}}{k_{z,j}}}} \tag{17}$$

$$A_n = \sum_{n=1}^{\infty} \frac{4Q\cos\left(\delta_n\sqrt{\frac{k_{x,j}}{k_{y,j}}}Y_c\right)\sin\left(\delta_n\sqrt{\frac{k_{x,j}}{k_{y,j}}}\frac{W_c}{2}\right)}{LWW_c\ k_{z,j}\delta_n^2\Phi(\delta)\sqrt{\frac{k_{x,j}}{k_{z,j}}}\sqrt{\frac{k_{x,j}}{k_{y,j}}}} \tag{18}$$

$$A_{mn} = \sum_{m=1}^{\infty}\sum_{n=1}^{\infty} \frac{16Q\cos(\lambda_m X_c)\cos\left(\delta_n\sqrt{\frac{k_{x,j}}{k_{y,j}}}Y_c\right)\sin\left(\lambda_m\frac{L_c}{2}\right)\sin\left(\delta_n\sqrt{\frac{k_{x,j}}{k_{y,j}}}\frac{W_c}{2}\right)}{LWL_cW_c\ k_{z,j}\ \lambda_m\delta_n\beta_{mn}\ \Phi(\beta)\sqrt{\frac{k_{x,j}}{k_{z,j}}}\sqrt{\frac{k_{x,j}}{k_{y,j}}}} \tag{19}$$

in which X_c and Y_c represent the location of the center of the component over the substrate as shown in Fig. 1(b). On the top surface of the substrate ($z_1 = 0$) Eq. (10) becomes:

$$\theta|_{z_1=0} = A_{00} + \sum_{m=1}^{\infty}\cos(\lambda_m x)A_m + \sum_{n=1}^{\infty}\cos\left(\delta_n\sqrt{\frac{k_{x,1}}{k_{y,1}}}y\right)A_n + \sum_{m=1}^{\infty}\sum_{n=1}^{\infty}\cos(\lambda_m x)\cos\left(\delta_n\sqrt{\frac{k_{x,1}}{k_{y,1}}}y\right)A_{m,n} \tag{20}$$

In case of multi-component configurations (Fig. 1(b)), the superimposition of effects holds [10]:

$$\theta = \sum_{i=1}^{N_c}\theta_i. \tag{21}$$

in which θ_i is the temperature excess contribution produced by the i-th component. The presented approach is general; the thermal problem in orthotropic ($k_x = k_y = k_{ip} \neq k_z$) and isotropic ($k_x = k_y = k_z$) substrates can be solved provided some simplifications to the proposed equations. For isotropic substrates refer to Appendix B. Isotropic configurations are accounted in the following sections to comply with the most common industrial applications.

3. Calculation of the thermal resistance R_t in pyramidal multilayer structures

The temperature distribution at the top surface (Eq. (20)) is necessary to calculate the total resistance R_t of an electronic component, that is used to characterize the configuration. For single-source scenarios, the total resistance is defined as:

$$R_t = \frac{\max(T) - T_{\text{amb}}}{Q} = \frac{\max(\theta_1|_{z_1=0})}{Q} \tag{22}$$

where $\max(\theta_1|_{z_1=0})$ is the peak value of temperature excess at the top layer at $z_1 = 0$ (see Fig. 1), and it is derived from Eq. (10). The total resistance

$$R_t = R_{1D} + R_{sp} \tag{23}$$

is the sum of a one-dimensional term (R_{1D}) that considers the conductive and the convective heat transfer in the substrate, and a spreading contribution R_{sp} that includes the remaining terms of the Fourier expansion series (see Eq. (10)). The spreading contribution is present whenever the heat introduced through a component surface (A_c) can travel towards a larger contact region A_{base}; if $A_c = A_{\text{base}}$, R_{sp} is null and $R_t = R_{1D}$. Eq. (23) cannot be used for multi-component arrangements. Instead, the use of the Influence Coefficient Method [16] is required to include the self-effect of the s-th component and the influence of the other N−1 remaining sources. From Eq. (10) and Eq. (21), the temperature excess in the centroid of the s-th component due to the i-th heat source is:

$$\theta_s = \sum_{i=1}^{N_c}\theta_i(X_{c,s}, Y_{c,s}, 0) = \sum_{i=1}^{N_c}Q_i f_{i,s} \tag{24}$$

where $f_{i,s}$ is an influence coefficient based on the compound properties and the geometrical characteristics of the ith component and Q_i is the heat introduced from i-th component. By using Eq. (24), the total resistance for the s-th component in a multi-source configuration becomes:

$$R_{t,s} = \frac{\theta_s}{Q_s} = \sum_{i=1}^{N_c}\frac{Q_i}{Q_s}f_{i,s} \tag{25}$$

For single-source scenarios, the Influence Coefficient Method reduces to Eq. (23).

Pyramidal structures are a particular case of multilayer compositions. An example is schematized in Fig. 3; subsequent layers differ in in-plane dimensions. In pyramidal configurations the N reference frames are not aligned along a vertical common edge of the substrate (Fig. 3(b)).

Since the in-plane footprint differs over at least two subsequent layers, the analytical model described in Section 2 needs to be extended. For pyramidal structures, the total component resistance R_t is written as the sum of three contributions [13]:

$$R_t = R_{1D} + R_{sp,1} + R_{sp,2} \tag{26}$$

R_{1D} is the one-dimensional resistance of the entire structure, and for single-component configurations is obtained from Eq. (16). In Eq. (26), $R_{sp,1}$ is approximated as the spreading resistance of a compound system of layers whose in-plane size is the area A_{pad} of the first uneven layer (Fig. 4(a)); $R_{sp,2}$ is computed by neglecting the first uneven layer pad, and by spreading the introduced heat Q over a different footprint $A_c \rightarrow$

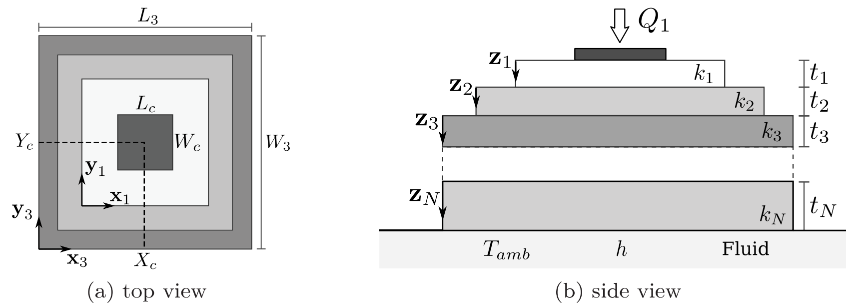

Fig. 3. Geometrical description of a discrete heat source (electrical component) mounted on top of a pyramidal compound substrate.

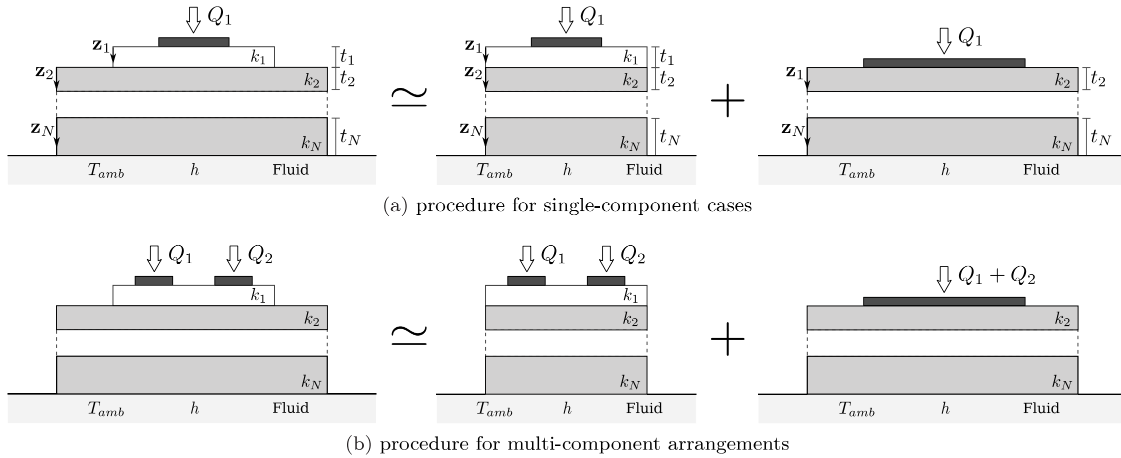

Fig. 4. Approximation method to calculate the total component resistance in pyramidal configurations.

Table 1
Characteristics of the powered electrical components used for experimental validation determined from information contained in [15].

Component (Fig. 5(b))	Q [W]	L_c [mm]	W_c [mm]	X_c [mm]	Y_c [mm]
Mosfet 1 (M1)	63.75	4.04	6.44	14.34	16.36
Mosfet 2 (M2)				20.32	16.36
Mosfet 3 (M3)	76.87			29.47	21.94
Mosfet 4 (M4)				35.50	21.94

Table 2
Thermophysical and geometrical properties of the compound substrate used for experimental validation.

Layer (Fig. 5(c))	Material	L [mm]	W [mm]	t [mm]	k [W/m K]
1	MOSFET solder	4.04	6.44	0.09	30
	DIODE solder	3.08	3.08		
2	copper	28.2	25.54	0.3	390
3	silicon nitride	28.2	25.54	0.32	90
4	copper	28.2	25.54	0.3	390
5	solder	28.2	25.54	0.2	30
6	baseplate	49.46	40.8	2.5	390
7	thermal grease	49.46	40.8	0.10	2.5
8	heat sink	49.46	40.8	30.77	237

A_{pad} (Fig. 4(a)). Two limit cases exist for the in-plane dimension of the first uneven layer: (1) if $A_{\text{pad}} = A_{\text{base}}$ the configuration of Section 3 is recovered; (2) if $A_{\text{pad}} = A_c$, then $R_{sp,1} = 0$ in Eq. (26).

The procedure can be extended to pyramidal configurations with multiple uneven layers (see Fig. 3). For multi-component arrangements (Fig. 4(b)), the Influence Coefficient Method (Section 3) is applied under the assumption of equal number of pad layers shared by each component on the top of a common substrate.

4. Validation: power module with pyramidal multilayer substrate

The analytical model is validated on a power module produced by Microsemi® (id APTMC120AM20CT1NG, see Fig. 5(a)), for which experimental measurements and 3D FEA simulations are available from the literature [15]. The substrate is modeled as proposed in Fig. 5(b). Information about the position of its four MOSFETs (M1, M2, M3 and M4) and the input power is collected in Table 1. The MOSFETs are grouped in couples over the x-direction; they have the same dimensions $L_c \times W_c$ = 4.04× 6.44 mm. While M1 and M2 introduce a power Q_1 = Q_2 = 63.75 W, the second couple is characterized by Q_3 = Q_4 = 76.87 W. The four diodes (marked D1 to D4) are passive elements.

The electronics lays on top of a multilayer structure that can be interpreted as a complex combination of Figs. 1(c) and 3(b) (Fig. 5(c)). More precisely, it is mounted via soldering on top of a direct bonded copper (DBC) construction. The DBC is composed of a layer of silicon nitride (t = 0.32 mm, k = 90 W/m K) in between two layers of copper (t = 0.3 mm, k = 390 W/m K). In turn, the DBC is soldered to a copper baseplate, whose thickness is 2.5 mm. The use of a thin layer of low-conductive thermal grease (t = 0.1 mm, k = 2.5 W/m K) allows to combine the substrate with an aluminum heat sink. The heat sink is cooled at its bottom to preserve a constant temperature T_{amb} = 325.75 K during the experimental analysis. From [15], the thickness of the heat sink is t = 30.77 mm. The constant temperature profile corresponds to a heat transfer coefficient $\bar{h} \to \infty$ in the proposed model. The properties of the different layer substrates are summarized in Table 2.

Experimental and numerical temperature profiles are compared on two axial lines (in yellow), as shown in Fig. 5(b): (a) CD spans vertically

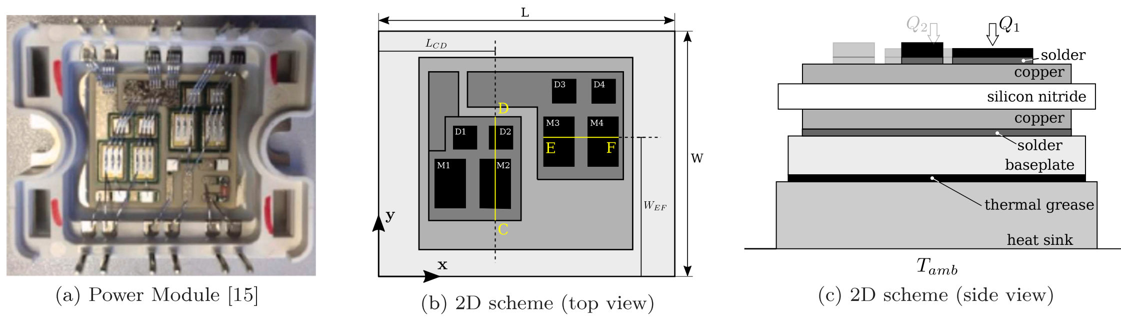

(a) Power Module [15] (b) 2D scheme (top view) (c) 2D scheme (side view)

Fig. 5. Top view of Microsemi® power module (PM) and simplified scheme adopted for experimental validation.

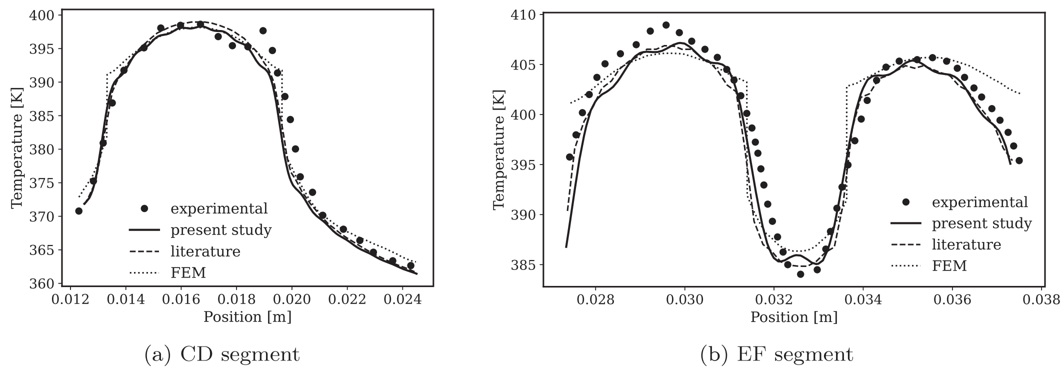

(a) CD segment (b) EF segment

Fig. 6. Code verification against experimental [15] and numerical (FEA) results for the PM test case; lines extrema in Table 3.

Table 3
Position of the extrema of the axial lines used to validate the PM test case.
Source: Information from [15].

Point (Fig. 5(b))	x [mm]	y [mm]
C	20.152	12.500
D	20.152	24.500
E	27.340	22.282
F	37.300	22.282

along M2, close to the center of the MOSFET; (b) EF spans horizontally, from the left side of M3 to the right side of M4, right above the centers of the pair. The location of each point is available in Table 3. Details about the experiments can be found in [15].

In the following (Figs. 6 and 7), results by the analytical model of Section 2 are labeled as *present study* and are compared against numerical results (3D FEA) and experimental values available from the literature [15] (Fig. 6). A good agreement is evidenced across MOSFET M1 (Fig. 6(a)), with the exception in correspondence of $y \simeq 0.019$ m, where experimental data are deteriorated by the wiring of the electronics [15]. Real geometrical dimensions of the MOSFET soldering are accounted in FEA simulations; this justifies the temperature behavior of the solution by FEA at $y \simeq 0.013$ m and $y \simeq 0.0195$ m. The effect is more apparent in Fig. 6(b); line EF starts on the left border of MOSFET M3 and ends on the right side of M4, which causes a strong difference in the temperature solution at point E and F.

The sum of the heights of the uneven layers equals 3.5% of the overall thickness of the substrate. Even though some of the thin layers have high conductivity, their small thickness prevents a high spreading. Hence, the shape of layers 1 to 5 can be extended to that of layers 6 to 8 without severely affecting the overall result. This is confirmed in Fig. 6 by comparing experimental and FEA results against solutions from the present method.

The relative error of temperature excess between the results from the analytical model and a reference solution is named $\mathrm{err}_{\theta,\mathrm{ref}}$ and is defined as follows:

$$\mathrm{err}_{\theta,\mathrm{ref}} = \frac{\left|\theta(X_{c,i}, Y_{c,i}, 0)_{\mathrm{model}} - \theta(X_{c,i}, Y_{c,i}, 0)_{\mathrm{ref}}\right|}{\max(\theta(X_{c,i}, Y_{c,i}, 0)_{\mathrm{model}}, \theta(X_{c,i}, Y_{c,i}, 0)_{\mathrm{ref}})} \cdot 100 \tag{27}$$

The reference solution either comes from experimental results (exp) or from three-dimensional simulations (3D). In Fig. 6(b), $\mathrm{err}_{\theta,\mathrm{exp}} = 2.08\%$ for MOSFET M3 and $\mathrm{err}_{\theta,\mathrm{exp}} = 0.59\%$ for MOSFET M4. On the other hand, considering other numerical solutions from the literature (3D FEA), $\mathrm{err}_{\theta,3D} = 0.34\%$ and $\mathrm{err}_{\theta,3D} = 0.56\%$ for MOSFET M3 and M4 respectively.

In Fig. 7, experimental and present study results are compared against those from three-dimensional Conjugate Heat Transfer simulations (3D CHT) obtained using a FV code [27]. In the 3D CHT simulations, each layer has been represented as a solid region with its own conductivity. Ad-hoc boundary conditions in the three-dimensional simulations were used to model: (a) the interfaces between the layers, to mimic Eqs. (13) and (14); (b) the externally applied heat power sources (see Eqs. (4) and (5)). 3D CHT simulations are performed on two different configurations, namely: (a) a PC, whose in-plane dimensions of the substrate are those of Table 2; (b) a SIPD, where all the layers have the same in-plane size of layer 8 of Table 2. Appreciable differences are reported only for MOSFET M4. The peak temperature difference between PC and SIPD for MOSFET M4 is 2.35%. Nonetheless, the solution from the analytical model lays between the two CHT results for both line CD and EF.

The temperature profile across the substrate (Fig. 8) is properly captured. Sensible temperature gradients are caused by low conductive layers (i.e. when the soldering, the thermal grease or the silicon

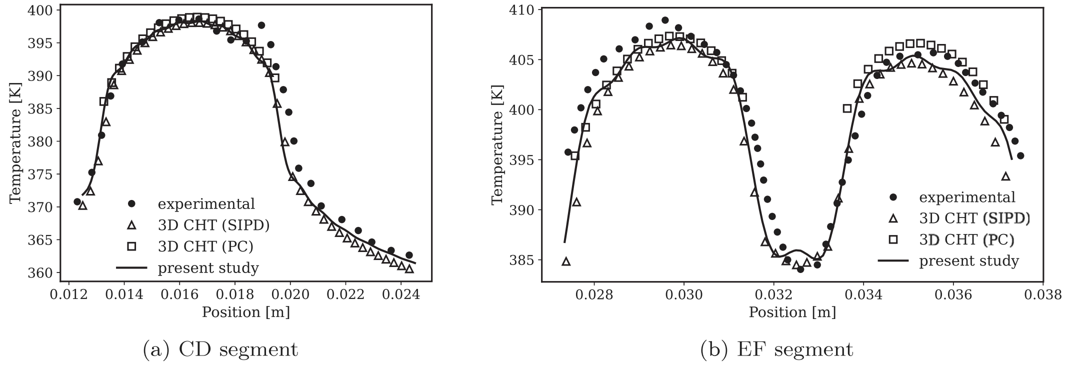

Fig. 7. Code verification against experimental [15] and numerical (3D CHT) results for the PM test case; lines extrema in Table 3.

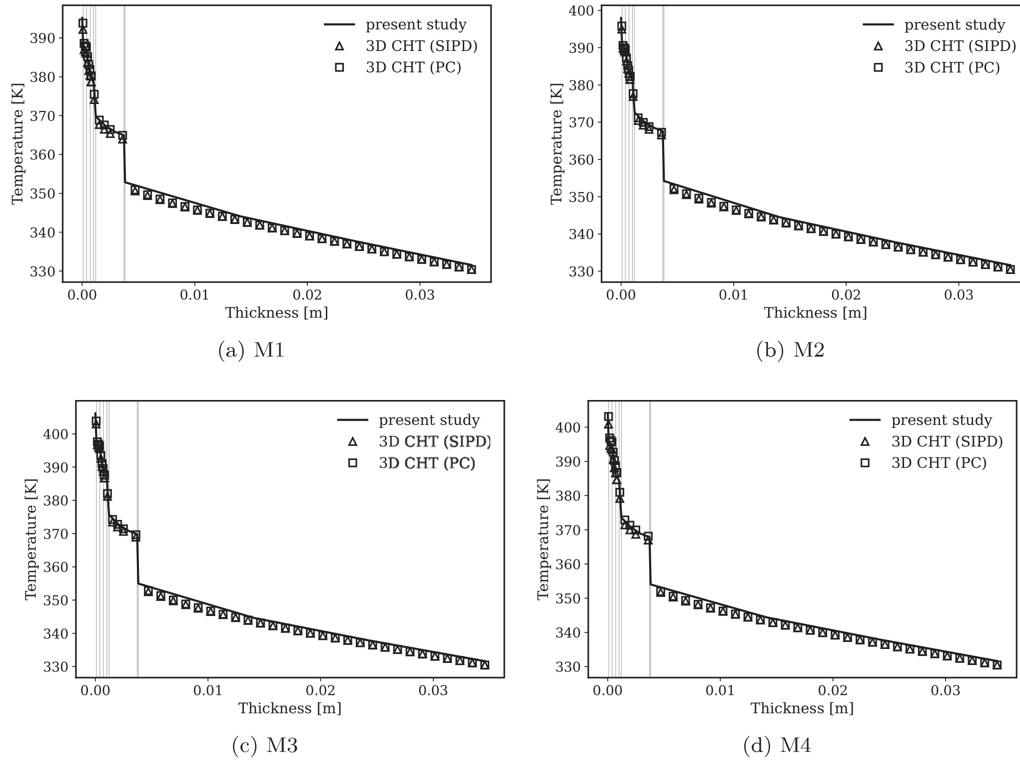

Fig. 8. Temperature evolution across the PM substrate via vertical lines passing through the center of each MOSFET; vertical gray lines mark layer-to-layer interfaces.

nitride are used). Results from three-dimensional simulations in Fig. 8 confirm that thin pyramidal layers of a compound substrate can be approximated as SIPD layers.

5. Multivariable optimization of multi-source multilayer arrangements

The calculation of the total resistance R_t in multi-source arrangements is the starting point of a multivariable optimization procedure. In this work, the summation of the total resistance of each component $R_{t,i}$ computed by the Influence Coefficient Method is selected as indicator of the thermal performance of the substrate. Since the overall total resistance is linked to the thermal stress of the components, it can be identified as the objective function to minimize:

$$R_{t,opt} = \min\left(\sum_{i=1}^{N_c} R_{t,i}\right) \tag{28}$$

Being the formulation dependent on multiple configuration variables, the multivariable problem described in Eq. (28) takes the form [28]:

$$\min\left(f(\mathcal{X})\right) \qquad \mathcal{X} \in \mathbb{R}^n \tag{29}$$

being:

$$\mathcal{X} = \mathcal{X}\left(\boldsymbol{X}_{c,i}, \boldsymbol{t}, \boldsymbol{k}, \boldsymbol{L}, \boldsymbol{W}, h\right) \tag{30}$$

In Eq. (30), $\boldsymbol{X}_{c,i}$ represents the two-dimensional location of the i-th component centroid on top of the substrate; $\boldsymbol{t}$ and $\boldsymbol{k}$ are respectively the vectors of layers thickness and thermal conductivity; $\boldsymbol{L}$ and $\boldsymbol{W}$ indicate the length and width of the substrate layers; h is the heat transfer coefficient. The objective functional $f : \mathbb{R}^n \rightarrow \mathbb{R}$ of the state $\mathcal{X}$ is subjected to some inequality constraints $g(\mathcal{X}) \leq 0$ with $g : \mathbb{R}^n \rightarrow \mathbb{R}^m$. These constraints bound each term $\mathcal{X}_i$ of the state $\mathcal{X}$ within admissibility regions. External limitations might come from production and industrial capabilities, as well as cost, encumbrance or weight. In particular, for the thickness of the j-th layer this implies:

$$t_{j,min} \leq t_j \leq t_{j,max} \qquad \forall j \in [1 : N] \tag{31}$$

Algorithm 1 multiVariableOptimizer

```
1:  XC = randomList(min,max)
2:  YC = randomList(min,max)
3:  x0, bounds = createBounds(XC(min,max),YC(min,max),L(min,max),W(min,max),t(min,max))
4:  finiteConductance = "interfacialHTC" in globals()          # finite conductance among layers
5:  if finiteConductance then
6:      # add finiteConductance to additional arguments (args)
7:  end if
8:  if SIPD then                                                 # same in-plane size
9:      minimizeFunction = minimizeSIPD
10: else                                                         # pyramidal configuration
11:     minimizeFunction = minimizePC
12: end if
13: res = minimize(minimizeFunction,x0,args=args,options=(tolerances),bounds=bounds,parallel)
```

and for the thermal conductivity:

$$k_{j,min} \leq k_j \leq k_{j,max} \qquad \forall j \in [1:N] \tag{32}$$

For other constraints, two different scenarios are considered, where the substrate layers have the *same in-plane dimensions* (SIPD) or involve a *pyramidal configuration* (PC) respectively. The length L and width W that define the geometry of compound systems whose layers share the SIPD are subjected to:

$$L_{min} \leq L \leq L_{max} \tag{33}$$

$$W_{min} \leq W \leq W_{max} \tag{34}$$

For *pyramidal configurations* (PC), both Eqs. (33) and (34) are layer-dependent:

$$L_{j,min} \leq L_j \leq L_{j,max} \qquad \forall j \in [1:N] \tag{35}$$

$$W_{j,min} \leq W_j \leq W_{j,max} \qquad \forall j \in [1:N] \tag{36}$$

Also, the position of the sources can be varied on the top surface of the substrate. Therefore, $X_{c,i}$ and $Y_{c,i}$ of all the N_c components are to be optimized. With reference to Fig. 1(b), the following is valid for SIPD configurations:

$$\frac{L_{c,i}}{2} \leq X_{c,i} \leq L - \frac{L_{c,i}}{2} \qquad \forall i \in [1:N_c] \tag{37}$$

$$\frac{W_{c,i}}{2} \leq Y_{c,i} \leq W - \frac{W_{c,i}}{2} \qquad \forall i \in [1:N_c] \tag{38}$$

For SIPD, L and W in Eqs. (37) and (38) are coupled to Eqs. (33) and (34) respectively. For PC, the component position is defined with respect to the bottom layer reference frame (see Fig. 3(a)), as this favors the calculation of the proposed three-term approximation function. However, each component must be contained in the in-plane footprint of the first layer. Therefore, L and W become L_1 and W_1 respectively in Eqs. (37) and (38) for pyramidal configurations (PC). For both scenarios, an average heat transfer coefficient $\bar{h}$ is applied at the lower surface of the bottom layer in the pack. In the case of free convection, a change of the in-plane substrate footprint has minor effects on the heat transfer coefficient, thus $\bar{h}$ can be assumed as constant throughout the optimization process. With forced convection, $\bar{h}$ might strongly change with the channel width [29–31]. In such cases, the variable heat transfer coefficient is added to the state vector $\mathcal{X}$.

The solution of Eq. (29) requires an iterative procedure; for a given iteration p, the state $\mathcal{X}^p$ tends to a minimum for $p \to \infty$. Since the objective function of Eq. (10) is twice continuously differentiable, the iterative Sequential Least-Squares Quadratic Programming (SLSQP) can be adopted under the mentioned constraints [28]. Another choice is given by the bounded Limited-Memory BFGS algorithm (L-BFGS-B) which stores a limited amount of data, and it is therefore suitable to manage large problems [32]. A summary of the implemented optimization process is reported in Algorithm 1.

6. Optimization procedure: validation tests

Five additional configurations of compound systems with multilayer substrates (see Table 4), sharing the same in-plane dimensions (SIPD) or with pyramidal configurations (PC) are selected to validate the optimization procedure:

(a) compound systems with layers sharing the same in-plane dimensions (SIPD):

- **Case A.** Baseline configuration to validate the optimization of both single-layer thickness and single-source relocation.
- **Case B.** Baseline test extended by a double-source double-layer configuration, to test the ability of the algorithm to optimize the substrate thicknesses and minimize the influence effects in multi-source relocation.
- **Case C.** Three-component three-layer configuration; the test is selected to study the ability of the method to find the optimal component relocation combined with in-plane resizing. The test is performed considering both constant and variable heat transfer coefficient of the heat sink.

(b) compound systems with layers defining pyramidal configurations (PC), namely:

- **Case D.** Single-source pyramidal scheme. This configuration is used to test the ability of the optimizer to reduce the overall resistance in pyramidal substrates.
- **Case E.** Pyramidal structure with five components, see Fig. 4(b). This case is representative for the optimization of multi-source configurations, typical of industrial applications.

Since experiments for validation are not available, a validation is proposed against three-dimensional Finite-Volume (FV) simulations accounting for Conjugate Heat Transfer (CHT) among the solid layers and the coolant. The three-dimensional setup used is the same of Section 4. In Table 5, a satisfying agreement between the approach presented in this work and three-dimensional simulations is observed for all the cases. Considering the PC cases, it appears that $\text{err}_{\theta,3D}$ (Eq. (27)) reduces from case D to case E when a three-term approximation for the spreading resistance of the pyramidal substrate is used (see Eq. (26)). Reasons are: (a) the in-plane dimension of the thermal pad is larger for case E; (b) a higher thermal power is dissipated over a wider surface in case E; (c) the first layer on top of the pyramidal configuration is thick and low conductive. This observation suggests that the three-term approximation of Eq. (26) provides reliable results in case of low conductive and thick pyramidal layers. Also, the proposed method computes the total resistance starting from the temperature distribution at each component centroid. This simplification poses minor concerns for separated components whose interaction is limited. When the interaction is stronger, the maximum temperature of each component may

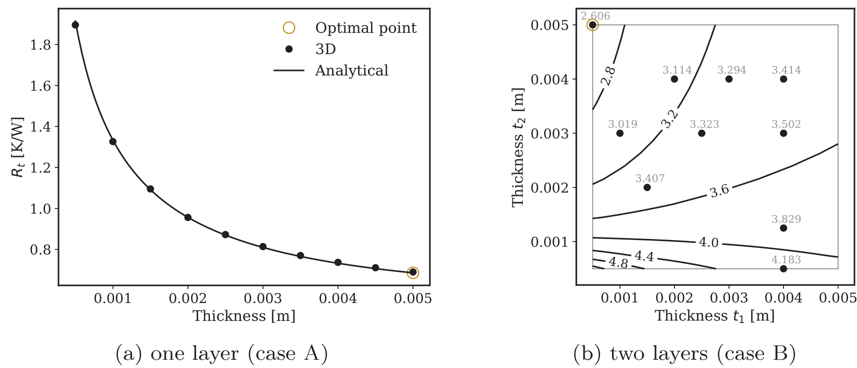

Fig. 9. Graphical validation of the thickness optimization process for the SIPD cases (A–C); brown circle is the optimal point; gray box in (b) defines the admissible region.

Table 4
Validation test-cases. Component position $(X_{c,i}, Y_{c,i})$ with respect to the bottom layer N. Information for multilayer packs is given from top to bottom (see Figs. 1(c) and 3(b)).

	Units	A	B	C	D	E
N_c	[–]	1	2	3	1	5
L_C	[mm]	18	[10; 10]	[10; 10; 10]	15	[40; 35; 28; 20; 20]
W_C	[mm]	15	[10; 10]	[10; 10; 10]	15	[32; 28; 20; 20; 28]
$X_{c,i}$	[mm]	21	[12; 45]	[13; 35; 55]	35	[60; 90; 120; 130; 155]
$Y_{c,i}$	[mm]	47	[48; 50]	[15; 35; 57]	35	[45; 80; 40; 65; 80]
Q_i	[W]	20	[15; 15]	[10; 10; 10]	20	[40; 30; 24; 16; 24]
pyramidal		✗	✗	✗	✓	✓
N	[–]	1	2	3	2	3
L	[mm]	70	[70; 70]	[70; 70; 70]	[20; 70]	[170; 200; 200]
W	[mm]	70	[70; 70]	[70; 70; 70]	[20; 70]	[100; 130; 130]
k_j	[W/m K]	200	[50; 200]	[10; 50; 100]	[20; 50]	[5; 100; 50]
t_j	[mm]	2	[2; 5]	[2; 3; 2]	[2; 3]	[1; 2; 3]
$\bar{h}$	[W/m² K]	500	500	900	925.42	1125.42
T_{amb}	[K]	298.15	298.15	298.15	338.15	338.15

not be located at the component center. To avoid this issue, it would be recommended to calculate the total resistance using the average temperature on the component footprint. In the current validation, for a fair comparison, total resistances calculated in Table 5 are extracted from three-dimensional simulations at the centroid of each heated surface.

Data of Table 4 are the starting point of the optimization procedure. The contribution to the optimal solution of the state parameters of Eq. (30) is discussed in the following.

6.1. Substrate thickness optimization

The first parameter studied is the j-th layer thickness t_j. In multi-layer scenarios this implies a dimension $N_v = N$. In case A, a single layer is present ($N_v = 1$). As expressed in Section 5, some constraints must be added. For each case, the limit $t \in [0.5 : 5]$ mm is set for each layer. The lower value represents a limit in industrial capabilities, the upper one combines limitations on encumbrance and weight. For the cases having same in-plane dimensions (cases A to C), results of the minimization procedure are summarized in Table 6, where the reduction of total resistance $R_{t,red}$ is calculated by comparing the initial configuration and the optimized one:

$$R_{t,red} = \frac{R_{t,opt} - R_{t,init}}{R_{t,init}} \cdot 100 \tag{39}$$

Because of the applied constraints, an admissible region is defined for the thickness of each material. The optimal layer thickness (or the optimal apportionment of the overall thickness among the layers) must lay in the admissible region (gray box in Fig. 9(b)). It is always possible to define a minimum point in the admissible region, either internal to it, or at the imposed boundaries (Fig. 9). To prove this assumption, Fig. 9(a) shows the optimal thickness value for case A; Fig. 9(b) depicts the same for case B, where the dimension of state $\mathcal{X}$ is $N_v = 2$. In Fig. 9(b) the value of the overall total resistance is proposed via isolines based on the variation of each layer thickness. The two figures contain also three-dimensional multi-region solutions (circular dots) to prove that the optimization process is predicting the overall best configuration with good accuracy. The results of Fig. 9 are obtained with the verified methodology of Section 3, and they match the solutions of the optimization process depicted in Section 5. The predominant factor that regulates the thickness apportionment is the thermal conductivity of the various layers in the pack. From Eq. (16), an increment of the layer thickness produces negative effects on R_{1D}. At the same time, if k_i of the i-th layer is sufficiently high, the increment of thickness helps the spreading of the introduced heat power: as a consequence, the peak of temperature and the sensed thermal stress [4] are reduced. It follows that the ordering of the layers in compound substrate is crucial to preserve low levels of thermal resistance.

Up to this point, the location of the components is preserved throughout the optimization procedure.

6.2. Optimization of substrate thickness and component repositioning

In some cases, the positions of the discrete heat sources are not prescribed or fixed. Component relocation is accounted in the optimizer to reduce thermal stress by minimizing cross-interactions among the sources. Starting from the initial conditions proposed in Table 4, the best location for the heat sources on the top surface of the substrate are indicated in Table 7. The results are graphically shown in Fig. 10.

The vector of the states $\mathcal{X}$ includes now a number of variables $N_v = N + 2N_c$. The thickness of each layer of the pack and the in-plane position of the components are modified during the optimization process; the SLSQP or the L-BFGS-B algorithm proceed to minimize the objective function (Eq. (28)). The resulting optimal apportionment of the thicknesses is unchanged compared to Table 6. In case A, the single component is moved to the center of the square substrate (Fig. 10(a)). More precisely, the single component is centered at the top surface regardless of the thermal conductivity of the layer and the initial guess of component location. By prescribing a set of random positions (X_c^0, Y_c^0) and thermal conductivities, the tool returns as optimal $X_c = L/2$ and $Y_c = W/2$. This position minimizes the spreading resistance, promotes radial heat diffusion, and exploits the constant heat transfer coefficient at the bottom of the substrate. With two electronic components (heat sources), the solution is influenced by multiple geometrical and thermal quantities. For this reason, case B is composed of two identical squared sources, on top of a squared isotropic substrate. To optimize case B, the two identical components are aligned along a diagonal of the squared substrate (Fig. 10(b)). Since the number of diagonal is 2, the number of optimal admissible solutions is 2; the sources are aligned over one of the two diagonals based on the initial conditions $(X_{c,i}^0, Y_{c,i}^0)$. The same

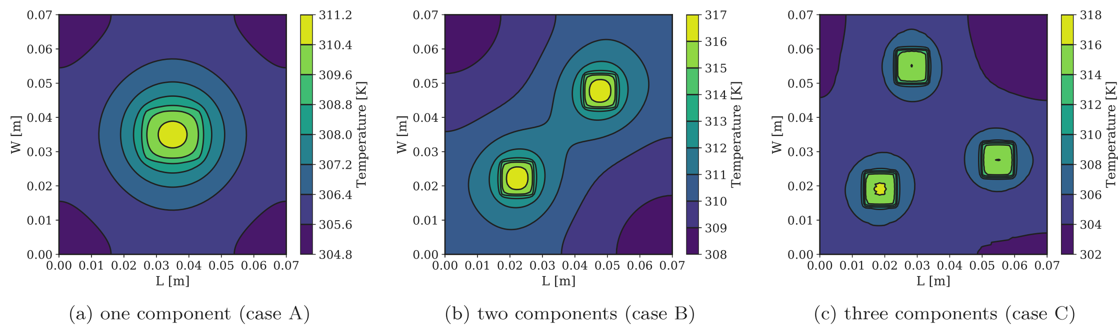

Fig. 10. Graphical view of the optimal component relocation for the SIPD cases (A–C) under the applied constraints.

Table 5
Numerical validation of the analytical model against 3D CHT results for *same in-plane dimensions* (SIPD) substrates (A–C) and *pyramidal configurations* (PC) substrates (D, E); temperature in [K], total resistance in [K/W], $err_{\theta,3D}$ from Eq. (27). Number of components N_c is case dependent (Table 4); no data available for $i > N_c$.

		T_1	$R_{t,1}$	T_2	$R_{t,2}$	T_3	$R_{t,3}$	T_4	$R_{t,4}$	T_5	$R_{t,5}$	$\max(err_{\theta,3D})$
Case A	Analytical	317.27	0.956				No data					0.21%
	3D	317.23	0.956									
Case B	Analytical	321.58	1.562	320.44	1.486			No data				0.63%
	3D	321.54	1.559	320.30	1.476							
Case C	Analytical	332.91	3.476	331.69	3.354	332.91	3.476		No data			1.67%
	3D	332.33	3.418	331.80	3.365	332.74	3.459					
Case D	Analytical	370.09	1.597				No data					1.91%
	3D	369.48	1.570									
Case E	Analytical	359.31	0.529	358.67	0.684	362.03	0.995	361.50	1.459	361.07	0.955	0.97%
	3D	359.31	0.529	358.47	0.677	362.08	0.997	361.45	1.456	360.87	0.947	

Table 6
Optimization of the layers thickness for the SIPD validation cases (A–C).

case	$t_{j,opt}$ [mm]	$R_{t,red}$ [K/W]
A	5	−28.24%
B	[0.5; 5]	−14.3%
C	[0.5; 0.5; 5]	−45.27%

Table 7
Layer thickness optimization plus optimal component relocation for the SIPD validation cases (A–C).

	Units	A	B	C
$X_{c,i}$	[mm]	35	[22.1; 47.9]	[15.2; 51.2; 42.0]
$Y_{c,i}$	[mm]	35	[22.1; 47.9]	[28.0; 18.8; 54.8]
$t_{j,opt}$	[mm]	5	[0.5; 5]	[0.5; 0.5; 5]
$R_{t,red}$	[K/W]	−34.30%	−19.45%	−47.60%

Table 8
Optimal resizing of the substrate for case C; results include component relocation and layer thickness optimization; $\bar{h}$ is constrained.

	Units	C
$X_{c,i}$	[mm]	[35.0; 105.0; 175.0]
$Y_{c,i}$	[mm]	[35.0; 35.0; 35.0]
L_{opt}	[mm]	210
W_{opt}	[mm]	70
$t_{j,opt}$	[mm]	[0.5; 0.5; 5]
$R_{t,red}$	[K/W]	−58.96%

observation holds for case C, where the three identical components are arranged in a symmetrical way with respect to the substrate in-plane diagonal (Fig. 10(c)). Thus, depending on the initial inputs, one of four possible arrangements is obtained. The choice of the objective function and of the constraints forces each component in the arrangement to lay on the top surface of the first layer (Section 5). Besides, the components cannot overlap. From a comparison between Tables 9 and 7, it results that an adequate component relocation enhances the reduction of the thermal stress.

6.3. Variable in-plane dimensions

During the design phase, as the components are relocated, the dimension of the substrate might be subjected to variations under encumbrance constraints. A further reduction of the thermal stress is obtained by allowing the in-plane geometry to expand. For this reason, L and W should be included in the list of variables to be optimized. Also, depending on the cooling system (e.g. air cooling, forced convection), the heat transfer coefficient at the substrate bottom may or may not be constrained. This is investigated in the following.

Constrained heat transfer coefficient. For SIPD rectangular compounds, one value of optimal length L and one of width W should be considered. Thus, $N_v = N + 2N_c + 2$. Starting from the configuration of case C depicted in Table 4 ($L = L_{init}$), the constraint applied to the length the substrate is now relaxed ($L \in [0.5L_{init} : 3L_{init}]$). The optimization process is repeated, and results are shown in Table 8 and Fig. 11.

With a constant and uniform value of the heat transfer coefficient at the bottom of the solid pack, the components are relocated to occupy the maximum admissible surface and to maximize their relative separation so as to reduce the cross-interactions on heat spreading. In particular, the Fourier terms in Section 2 are written to be insensitive to the flow direction of the fluid in the below cooling channel. As the heat transfer coefficient at the bottom of the substrate is considered homogeneous and constant, the reshape of the substrate is influenced by: (a) the minimum and maximum limits for L and W imposed to the layers; (b) the need to minimize the overall thermal resistance R_{tot} according to the objective function (Eq. (28)); (c) the initial state (i.e. the initial position of the electrical components on the substrate). Two optimal solutions would be admissible: (a) $W_{opt} = W_{init}$, $L_{opt} = 3L_{init}$ and (b)

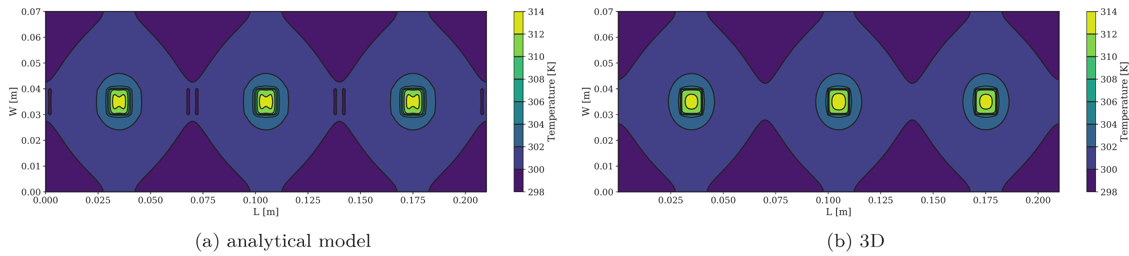

Fig. 11. Graphical view of the optimal case C configuration upon component relocation, in-plane resizing, and layer thickness optimization; $\bar{h}$ is constrained.

Table 9
Optimal resizing of the substrate for case C; results include component relocation and layer thickness optimization; $\bar{h}$ varies with the in-plane footprint.

	Units	C
$X_{c,i}$	[mm]	[17.5; 52.5; 87.5]
$Y_{c,i}$	[mm]	[17.5; 17.5; 17.5]
L_{opt}	[mm]	105
W_{opt}	[mm]	35
$t_{j,opt}$	[mm]	[0.5; 0.5; 5]
$\bar{h}_{opt}$	[W/m^2 K]	1906.41
$R_{t,red}$	[K/W]	−56.92%

$W_{opt} = 3W_{init}$, $L_{opt} = L_{init}$. The behavior of the two configurations is the same. Only the second one can be accepted because only L is allowed to vary, and is the one returned by the optimization procedure. For the considered scenario, the geometry of the substrate has changed, the three components are relocated (Fig. 11), but the apportionment of thickness among the layers is unchanged with respect to Table 6. Overall, the accuracy of the prediction of the temperature distribution at the top surface is satisfying (Fig. 11); the same is true for the total resistance of the three components. Minor discrepancies in Fig. 11 are due to meshing and truncation of the Fourier's series. The applied relaxation on the in-plane size has severely reduced the overall thermal stress.

Unconstrained heat transfer coefficient. To extend the analysis, the solution proposed in Table 9 and Fig. 12 considers forced convection with unconstrained heat transfer coefficient $\bar{h} = f(Re, Nu, Pr)$ (being Re, Nu and Pr the Reynolds, Nusselt and Prandtl numbers respectively) and $L \in [0.5L_{init} : 1.5L_{init}]$, $W \in [0.5W_{init} : 1.5W_{init}]$. It is important to note that the form the Laplace's heat equation is written (and the Fourier expansion series approximating it) is in principle insensitive to the flow direction of the fluid in the cooling channel. Under the assumptions [30,31,33] of: (a) constant thermophysical properties of the flow at the working temperature in the cooling channel considered in this study; (b) cross section of the cooling channel equal to W×t (the channel is oriented as the x direction, see Figs. 1(b) and 1(c)), it follows that:

$$\bar{h} = f(Re, Nu, Pr) = \bar{h}(Re) = \bar{h}(U, W, t) \tag{40}$$

where U is the flow velocity. For a given flow rate $U \cdot W \cdot t =$ const, if the channel height t is constant, the flow velocity is dependent on the channel width only, so $\bar{h} = \bar{h}(W)$. Being the channel width W modified by the optimizer, the heat transfer coefficient varies and so the reshaping; in this sense, direction of flow motion force works as a constraint for the optimization procedure. The same conclusion does not hold if constrained heat transfer coefficient ($\bar{h} = const$) at the bottom of the substrate is used. Results of Table 9 show the effect of forced fluid convection: $L_{opt} = 1.5L_{init}$, $W_{opt} = 0.5W_{init}$, and $\bar{h}_{opt} = 1906.41$ W/m^2 K. The components are arranged in the same way as in Fig. 11, the thickness apportionment is unchanged with respect to Table 6, but the remaining state-variables differ from those of Table 7.

Table 10
Optimization of the layers thickness for the PC validation case D.

	Units	D
$X_{c,i}$	[mm]	35
$Y_{c,i}$	[mm]	35
$t_{j,opt}$	[mm]	[0.5; 5]
$R_{t,red}$	[K/W]	−30.50%

Table 11
Optimization of the layers thickness for the PC validation case D plus optimal in-plane resizing under the applied constraints.

	Units	D
$X_{c,i}$	[mm]	52.5
$Y_{c,i}$	[mm]	52.5
L_{opt}	[mm]	[30; 105]
W_{opt}	[mm]	[30; 105]
$t_{j,opt}$	[mm]	[0.5; 5]
$R_{t,red}$	[K/W]	−33.87%

6.4. Layer structure

Two cases are investigated, namely case D and E. They are discussed in the following.

Case D. The two-layer single-component test serves to assert the accuracy of the method shown in Section 3 against three-dimensional multi-region simulations. The component is already centered in the top pad. As the top pad is at the center of the bottom layer, the component position is already optimized. The minimization process confirms this assumption, while it varies the thickness of the two solid sheets. The optimized configuration is proposed in Table 10.

The optimal apportionment of the overall solid thickness promotes a reduction of thermal resistance: $R_{t,red} = -30.50\%$ for case D. Fig. 13 allows to compare the temperature distribution at top surface obtained via the analytical model with the one from a three-dimensional multi-region simulation. The error on the peak temperature excess is $\text{err}_{\theta,3D} = 0.21\%$ (Eq. (27)). When the thickness of the top low conductive thermal pad is much smaller than that of the remaining high conductive materials, an approximation is valid: the pyramidal structure can be transformed into a SIPD rectangular substrate. For test case D in its optimized configuration, this approximation returns an error $\text{err}_{\theta,3D} \simeq 0.15\%$.

By allowing the in-plane dimensions to be resized, the component gets relocated at the center of the new enlarged substrate (Table 11). If the in-plane size can scale up to 1.5X the initial dimensions, the volume of the layers increases. Even though this has a negative effect on the spreading resistance, the one-dimensional contribution decreases enough to guarantee an overall reduction of the thermal stress. For the new configuration proposed in Fig. 14, the thermal stress reduction is $R_{t,red} = -33.87\%$ (Table 11).

Case E. Case E is an example of an industrial-like configuration. In case E, multiple components of different size are mounted on top of a

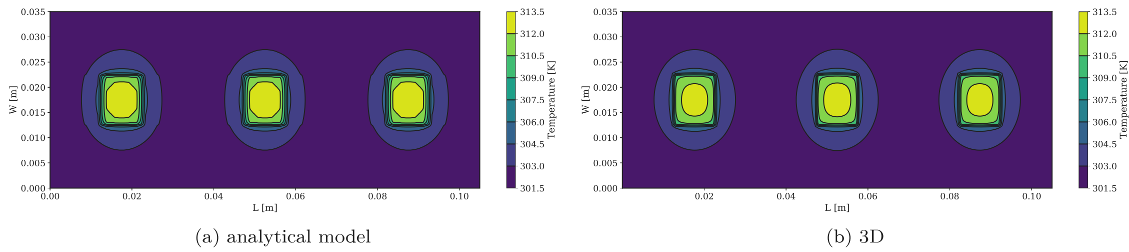

Fig. 12. Graphical view of the optimal case C configuration upon component relocation, in-plane resizing, and layer thickness optimization; $\bar{h}$ varies with the in-plane footprint.

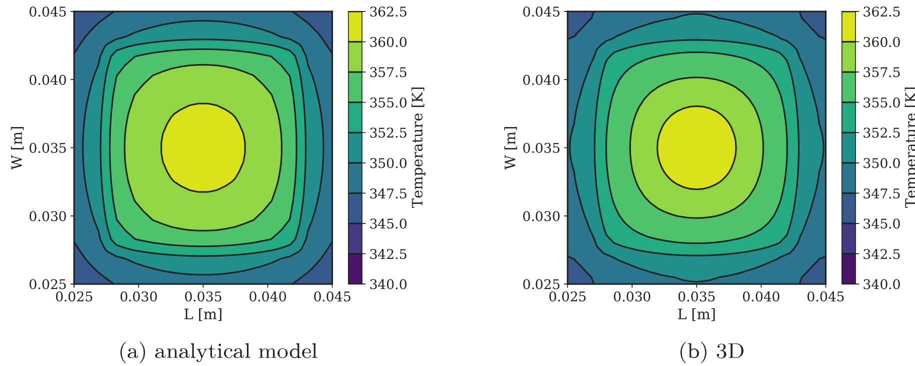

Fig. 13. Graphical view of the PC validation case D upon optimization of the layers thickness.

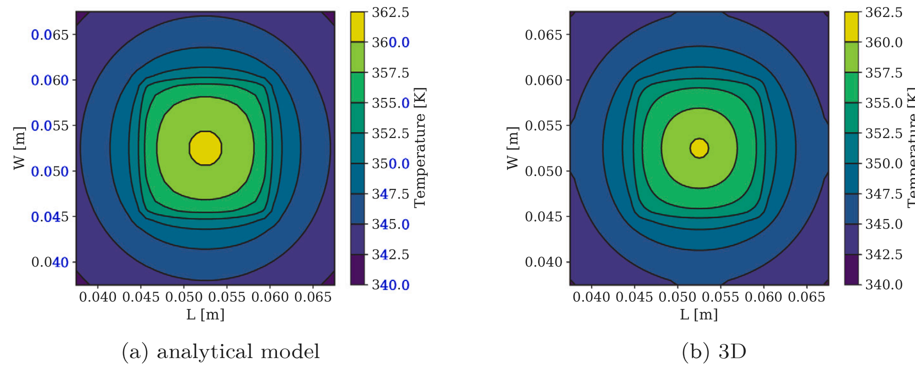

Fig. 14. Graphical view of the PC validation case D upon optimization of the layers thickness and in-plane resizing.

multilayer pyramidal structure. The temperature distribution obtained via the analytical approach is compared against that obtained with three-dimensional multi-region analysis. With respect to case D, the smaller discrepancy of in-plane dimensions between uneven layers and the higher amount of heat introduced from the top help to reduce $err_{\theta,3D}$. For this reason, a good agreement is also noted in Fig. 15, where the initial configuration is shown. The component relocation leads to the optimized arrangement proposed in Fig. 16. The results of temperature distribution produced via the analytical model are in good agreement with the reference for the optimized configuration as well. The component relocation and the optimal apportionment of the overall thickness permit to reduce the thermal stress: $R_{t,red} = -36.17\%$. The optimal geometrical properties are reported in Table 12.

Table 12
Optimization of the layers thickness and optimal component relocation for the PC validation case E.

	Units	E
$X_{c,i}$	[mm]	[47.6; 48.4; 111.0; 111.8; 162.4]
$Y_{c,i}$	[mm]	[39.6; 90.5; 39.4; 90.5; 68.4]
$t_{j,opt}$	[mm]	[0.5; 5; 5]
$R_{t,red}$	[K/W]	−36.17%

7. Convergence and computational speed of the optimization process

Eq. (28) is solved by the Sequential Least-Squared Quadratic Programming (SLSQP); the limited memory BFGS bounded algorithm (L-BFGS-B) returns similar solutions for all the considered tests. Convergence to an optimized configuration is always achieved, provided that state variables are bounded. The rate of convergence for the k-th iteration is defined as:

$$\left|\Delta R_t\right| = \left|R_t^k - R_t^{k-1}\right| \tag{41}$$

and it is reported for the different test cases in Fig. 17.

At the beginning of the optimization process $\left|\Delta R_t\right| = 1$. For all the tested cases, multiple simulations have been performed by varying the initial state variables. The initial position of the components and the thickness of each layer are selected as input in Fig. 17. Inputs are randomly selected within the admissible regions defined by the applied constraints. For this reason, the number of iterations required for

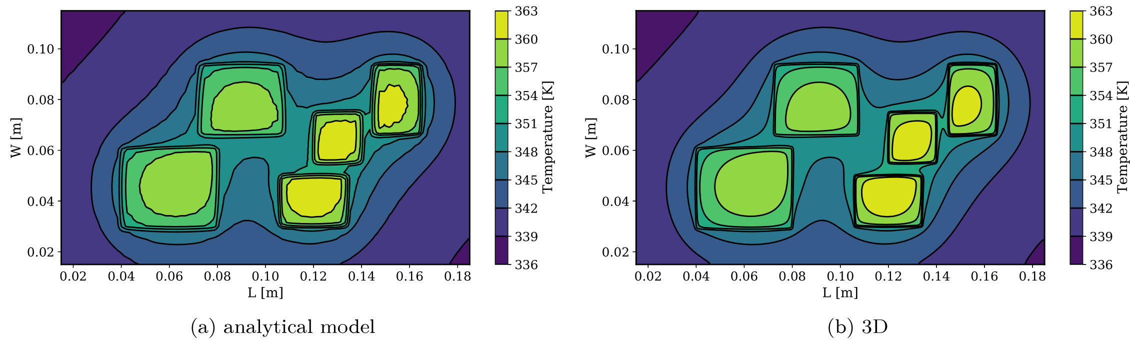

Fig. 15. Initial conditions for pyramidal configuration of case E.

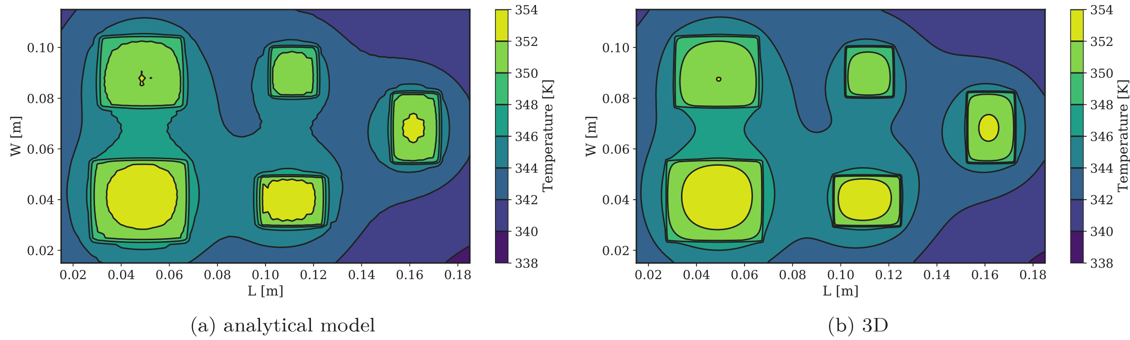

Fig. 16. Optimized arrangement of the electronics for the pyramidal configuration of case E.

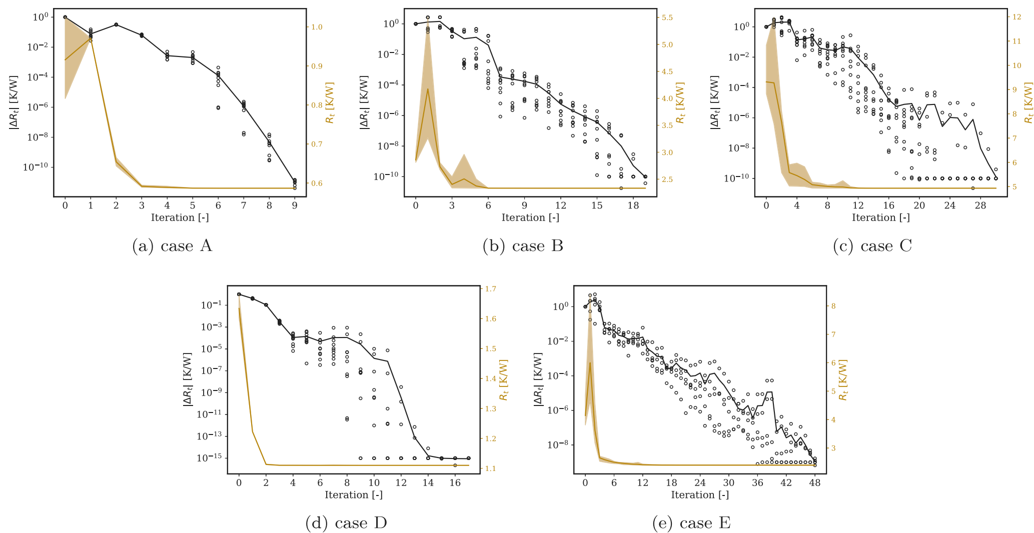

Fig. 17. Rate of convergence of the optimization process (black); objective function value (brown); lines are average.

convergence differs from case to case. The overall number of iterations increases as the numbers of sources and layers grows: at convergence, the value of the objective function is always smaller than that at the beginning. The objective function always reduces to a minimum plateau after few iterations. High rate of convergence is noted at the first few iterations (Fig. 17); the optimization process continues along just because of the strict tolerances set.

The overall computational time increases with the number of iterations. Nonetheless, the speed of the optimization process is satisfying. The methodology proves to be quicker than FEA and CFD three-dimensional multi-region simulations. This procedure lacks the complex pre- and post-processing that is common in CFD calculations; it does not require the coupling with a third-party optimizer; it avoids the repetition of the meshing procedure to comply with variations of the geometry and/or component relocation. Compared to neural networks and genetic algorithms, no time is spent on dataset training, or tuning of constant for evolution through generations, thus preserving the general applicability of the approach.

To fasten the proposed procedure even more, the optimization can be performed in parallel on multiple CPU cores [34] (Fig. 18(b)). The computational time taken to complete the optimization process on the proposed test cases is shown in Fig. 18 based on the number of variables contained in the state vector $\mathcal{X}$. Variable thickness of the solid layers, variable in-plane resizing and component relocation are

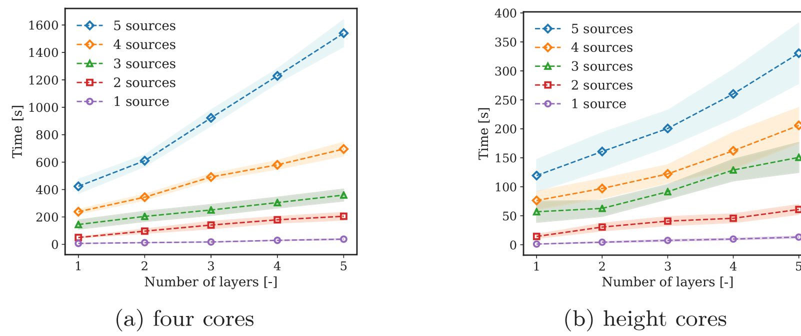

(a) four cores (b) height cores

Fig. 18. Computational time required by the optimization process depending on the CPU architecture; dimension of $\mathcal{X}$ is N_v and depends on N and N_c.

all taken into consideration to increase the number of variables. The architecture used for code validation ranges from a 4-core i7-8565U CPU and 16 Gb of RAM to a 8-core i9-9900k CPU and 32 Gb of RAM. Another relevant source of speed-up comes from the symmetrical nature of the influence coefficient matrix. By exploiting this property, the number of required operations is severely reduced. Major effects on the computational cost come from the truncation of the Fourier series that characterize Eq. (10); nonetheless, a variation of this parameter has some influence on the accuracy of the results. For the current analysis and validation, $m, n = 101$. Finally, the choice of less stringent tolerances for the minimization methods helps to reduce the number of iterations required to obtain convergence, thus decreasing the overall computational cost, and enhancing the speed-up.

8. Conclusions

An analytical model based on closed-form expressions structured on Fourier expansion series is presented to solve the thermal problem in multilayer substrates. For pyramidal schemes a three-term approximation function is coupled with the Influence Coefficient Method to predict the thermal resistance in multi-source pyramidal compound packs. The reliability of the model is demonstrated by a validation against experimental and three-dimensional FEA and FV results of (a) peak temperature and resistance of the electronics for multilayer rectangular and pyramidal substrates; (b) temperature distribution across the SIPD and PC compound pack and over the upper surface of the configurations. The model has been then included in a multivariable process to determine the optimal size and positioning of the discrete heat sources on electronic boards of electric motors. In the optimizer, the total thermal resistance of the configuration is used as objective function to minimize. The SLSQP or L-BFGS-B algorithms are chosen to extract the optimal point under the application of external inequality constraints. They combine limited cost, short execution time and low memory requirements. It is shown that an optimal relocation and apportionment of the overall thickness of the multilayer substrate promotes a sensible reduction of the thermal stress. It is also shown that the in-plane dimension of thin pyramidal layers at the top of compound structures can be approximated as that of the below heat sink.

The proposed method is still subjected to some limitations in geometrical shape of the substrates, that could be overcome by the application of the Quadrupole method; besides, shape optimization of the cooling channel could be done by the minimization of entropy losses. These aspects are out of the scope for the present analysis and are part of a work currently under development.

Declaration of competing interest

The authors declare that they have no known competing financial interests or personal relationships that could have appeared to influence the work reported in this paper.

Data availability

Data will be made available on request.

Appendix A. Two-dimensional temperature distribution at different vertical positions

The temperature distribution in an anisotropic compound system with layers having equal in-plane dimensions is described by Eq. (10). The bi-dimensional distribution of temperature at the top surface of the substrate ($z_1 = 0$) is obtained via Eq. (20), thanks to a loop on the spreading functions (see Section 2). A more complex numerical loop is shown here to describe the behavior of the temperature at other vertical quotes because of the spreading effects from the source plane. For instance, the temperature distribution at the top surface of the second layer is obtained from the boundary condition of perfect adhesion at the layer-to-layer interface:

$$\theta_1(x, y, z_1 = t_1) = \theta_2(x, y, z_2 = 0) \tag{42}$$

From Eq. (10), the explicit form of Eq. (42) is:

$$\begin{aligned}
&A_{00,1} + B_{0,1}\sqrt{\frac{k_{x,1}}{k_{z,1}}}t_1 + \sum_{m=1}^{\infty}\cos(\lambda_{m,1}x)A_{m,1}\left[\cosh(\lambda_{m,1}t_1) - \Phi_1(\lambda_{m,1})\sinh(\lambda_{m,1}t_1)\right] \\
&+ \sum_{n=1}^{\infty}\cos\left(\delta_{n,1}\sqrt{\frac{k_{x,1}}{k_{y,1}}}y\right)A_{n,1}\left[\cosh\left(\delta_{n,1}\sqrt{\frac{k_{x,1}}{k_{z,1}}}t_1\right) - \Phi_1(\delta_{n,1})\sinh\left(\delta_{n,1}\sqrt{\frac{k_{x,1}}{k_{z,1}}}t_1\right)\right] \\
&+ \sum_{m=1}^{\infty}\sum_{n=1}^{\infty}\cos(\lambda_{m,1}x)\cos\left(\delta_{n,1}\sqrt{\frac{k_{x,1}}{k_{z,1}}}y\right)A_{mn,1}\left[\cosh\left(\beta_{mn,1}\sqrt{\frac{k_{x,1}}{k_{z,1}}}t_1\right) - \Phi_1(\beta_{mn,1})\sinh\left(\beta_{mn,1}\sqrt{\frac{k_{x,1}}{k_{z,1}}}t_1\right)\right] \\
&= A_{00,2} + \sum_{m=1}^{\infty}A_{m,2}\cos(\lambda_{m,2}x) + \sum_{n=1}^{\infty}A_{n,2}\cos\left(\delta_{n,2}\sqrt{\frac{k_{x,2}}{k_{y,2}}}y\right) \\
&+ \sum_{m=1}^{\infty}\sum_{n=1}^{\infty}A_{mn,2}\cos(\lambda_{m,2}x)\cos\left(\delta_{n,2}\sqrt{\frac{k_{x,2}}{k_{y,2}}}y\right)
\end{aligned} \tag{43}$$

Based on the fact that:

$$\lambda_{m,1} = \lambda_{m,2} \tag{44}$$

$$\delta_{n,1}\sqrt{\frac{k_{x,1}}{k_{y,1}}}y = \frac{n\pi}{W}\sqrt{\frac{k_{y,1}}{k_{x,1}}}\sqrt{\frac{k_{x,1}}{k_{y,1}}}y = \frac{n\pi}{W}\sqrt{\frac{k_{y,2}}{k_{x,2}}}\sqrt{\frac{k_{x,2}}{k_{y,2}}}y = \delta_{n,2}\sqrt{\frac{k_{x,2}}{k_{y,2}}}y \tag{45}$$

the common terms are collected, and it holds:

$$A_{00,2} = A_{00,1} + B_{0,1}\sqrt{\frac{k_{x,1}}{k_{z,1}}}t_1 = \frac{Q}{LW}\left(\frac{1}{h} + \sum_{j=2}^{N}\frac{t_j}{k_{z,j}}\right) \tag{46}$$

$$A_{m,2} = A_{m,1}\left[\cosh\left(\lambda\sqrt{\frac{k_{x,1}}{k_{z,1}}}t_1\right) - \Phi_1(\lambda)\sinh\left(\lambda\sqrt{\frac{k_{x,1}}{k_{z,1}}}t_1\right)\right] \quad (47)$$

$$A_{n,2} = A_{n,1}\left[\cosh\left(\delta\sqrt{\frac{k_{x,1}}{k_{z,1}}}t_1\right) - \Phi_1(\delta)\sinh\left(\delta\sqrt{\frac{k_{x,1}}{k_{z,1}}}t_1\right)\right] \quad (48)$$

$$A_{mn,2} = A_{mn,1}\left[\cosh\left(\beta\sqrt{\frac{k_{x,1}}{k_{z,1}}}t_1\right) - \Phi_1(\beta)\sinh\left(\beta\sqrt{\frac{k_{x,1}}{k_{z,1}}}t_1\right)\right] \quad (49)$$

Also, for each layer $j \in [1 : N]$ the following is valid:

$$B_{i,j} = -\Phi_j(\gamma)A_{i,j} \quad (50)$$

where γ is λ, δ, β for $i = m, n, mn$ respectively. Hence, the spreading function loop presented in Section 2 is necessary to compute the temperature distribution at top surface, which in turn is used to evaluate the bi-dimensional distribution at different quotes. An iterative procedure permits to generalize the treatment to every layer of the compound substrate (Fig. 2). For a vertical position $z_p \in [0, t_p]$ in the p-th layer of the compound system, the Fourier coefficients A_i are:

$$A_{i,p} = A_{i,1}\prod_{j=1}^{p}\left[\cosh\left(\gamma\sqrt{\frac{k_{x,j}}{k_{z,j}}}t_j\right) - \Phi_j(\gamma)\sinh\left(\gamma\sqrt{\frac{k_{x,j}}{k_{z,j}}}t_j\right)\right] \quad (51)$$

A brief summary of the implementation is provided in Algorithm 2. Orthotropic and isotropic configurations are treated by means of simplifications.

Algorithm 2 verticalTemp

```
1: # select the in-plane position for the vertical axial line
2: for l in layers do
3:     kx = kVectX[l]; ky = kVectY[l]; kz = kVectZ[l]
4:     sum = 0
5:     for i in range(len(tVect[l:])) do
6:         sum ← # compute 1D resistance
7:         sum ← # add finite conductance resistance if present
8:     end for
9:     width = np.linspace(0,tVect[l],nSlices)
10:    for t in width do
11:        result = T0
12:        for source in range(len(Q)) do
13:            # compute A00, B00
14:            A1 = 0; A2 = 0; A3 = 0;
15:            for idx in range(1,101) do
16:                # calc Am (and correspondent Bm) in top layer
17:                A1 ← # loop for layer in range(0,l) and update Am
       and Bm
18:                A2 ← # repeat the operation for An, Bn
19:                for idx2 in range(1,101) do
20:                    A3 ← # repeat the operation for Amn, Bmn
21:                end for
22:            end for
23:            result += A00 + B00*sqrt(kx,kz)*t + A1 + A2 + A3
24:        end for
25:        # append result to an overall axial line vector
26:    end for
27: end for
```

Appendix B. Temperature distribution in isotropic substrates

The anisotropic analytical solution (Eq. (10)) can be simplified into the isotropic one. Based on the assumptions made in Section 2 about the geometry proposed in Fig. 1, the temperature excess in isotropic compound systems is regulated by the isotropic steady-state heat conduction equation:

$$\nabla^2\theta = \frac{\partial^2\theta}{\partial x^2} + \frac{\partial^2\theta}{\partial y^2} + \frac{\partial^2\theta}{\partial z^2} = 0 \quad (52)$$

On the source plane, the following BC substitutes Eq. (5):

$$-k_1\frac{\partial\theta_1}{\partial z}\bigg|_{z_1=0} = q \qquad (x,y) \in A_c \quad (53)$$

$q = 0$ elsewhere. For the Nth layer, the convective boundary condition becomes:

$$\frac{\partial\theta_N}{\partial z}\bigg|_{z_N=t_N} = -\frac{\bar{h}}{k_N}\theta_N(x,y,t_N) \quad (54)$$

The solution of Eq. (52) written in terms of Fourier expansion series after a variable separation is:

$$\theta = \sum_{m=1}^{\infty}\sum_{n=1}^{\infty} C(\lambda,\delta)e^{\lambda x}e^{\delta y}e^{i\sqrt{\lambda^2+\delta^2}z} \quad (55)$$

The application of Eq. (6) to Eq. (55) produces [4]:

$$\begin{aligned}\theta = {} & A_{00} + B_0 z + \sum_{m=1}^{\infty}\cos(\lambda_m x)\left[A_m\cosh(\lambda_m z) + B_m\sinh(\lambda_m z)\right] \\ & + \sum_{n=1}^{\infty}\cos(\delta_n y)\left[A_n\cosh(\delta_n z) + B_n\sinh(\delta_n z)\right] \\ & + \sum_{m=1}^{\infty}\sum_{n=1}^{\infty}\cos(\lambda_m x)\cos(\delta_n y)\left[A_{mn}\cosh(\beta_{mn}z) + B_{mn}\sinh(\beta_{mn}z)\right]\end{aligned} \quad (56)$$

for which $\lambda_m = \frac{m\pi}{L}$, $\delta_n = \frac{n\pi}{W}$ and $\beta_{mn} = \sqrt{\lambda_m^2 + \delta_n^2}$.

In the case of perfect adhesion between subsequent layers, the Fourier's coefficients are:

$$B_0 = -\left(\frac{\bar{h}}{k_N + \bar{h}t_N}\right)A_{00} \quad (57)$$

$$B_{i,N} = -\left(\frac{\bar{h} + k_N\gamma\tanh(\gamma t_N)}{\bar{h}\tanh(\gamma t_N) + k_N\gamma}\right)A_{i,N} = -\Phi_N(\gamma)A_{i,N} \quad (58)$$

$$B_{i,j} = -\left(\frac{\tanh(\gamma t_j) + \Phi_{j+1}(\gamma)\frac{k_{j+1}}{k_j}}{1 + \Phi_{j+1}(\gamma)\frac{k_{j+1}}{k_j}\tanh(\gamma t_j)}\right)A_{i,j} = -\Phi_j(\gamma)A_{i,j} \quad (59)$$

where γ is λ, δ, β for $i = m, n, mn$ respectively. Also:

$$A_{00} = \frac{Q}{LW}\left(\frac{1}{\bar{h}} + \sum_{j=1}^{N}\frac{t_j}{k_j}\right) \quad (60)$$

$$A_m = \sum_{m=1}^{\infty}\frac{4Q\cos(\lambda_m X_c)\sin\left(\lambda_m\frac{L_c}{2}\right)}{LWL_c\ k_j\lambda_m^2\Phi(\lambda)} \quad (61)$$

$$A_n = \sum_{n=1}^{\infty}\frac{4Q\cos(\delta_n Y_c)\sin\left(\delta_n\frac{W_c}{2}\right)}{LWW_c\ k_j\delta_n^2\Phi(\delta)} \quad (62)$$

$$A_{mn} = \sum_{m=1}^{\infty}\sum_{n=1}^{\infty}\frac{16Q\cos(\lambda_m X_c)\cos(\delta_n Y_c)\sin\left(\lambda_m\frac{L_c}{2}\right)\sin\left(\delta_n\frac{W_c}{2}\right)}{LWL_cW_c\ k_j\ \lambda_m\delta_n\beta_{mn}\ \Phi(\beta)} \quad (63)$$

Appendix C. Optimal component relocation in the case of inhomogeneous heat transfer

A simplification was made in Section 2 to consider an homogeneous heat transfer coefficient $\bar{h}$ at the bottom of the substrate. However, satisfying results can also be obtained in the case of inhomogeneous heat transfer coefficients at the heat sink ($h(x,y)$) thanks to the proposed methodology. By considering case A of Table 4 and the $h(x)$ of Fig. 19(a), it is expected the single component to be relocated according to the minimization of the summation of the one-dimensional and spreading contributions of the resistance.

Indeed, the component is relocated in a different position with respect to that presented as optimal in Table 7 where convection was homogeneous. The source is moved on top of the eccentric stripe which corresponds to the higher convection cooling (Fig. 19(c)). To

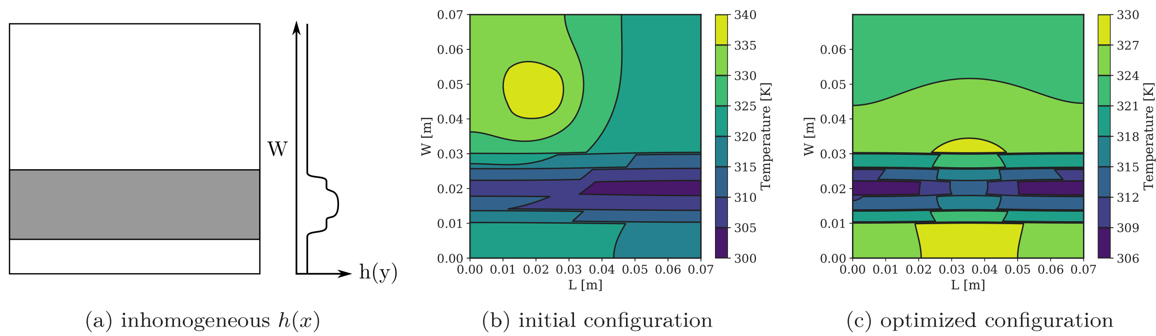

Fig. 19. Electrical component relocation in the case of one-dimensional inhomogeneous convection.

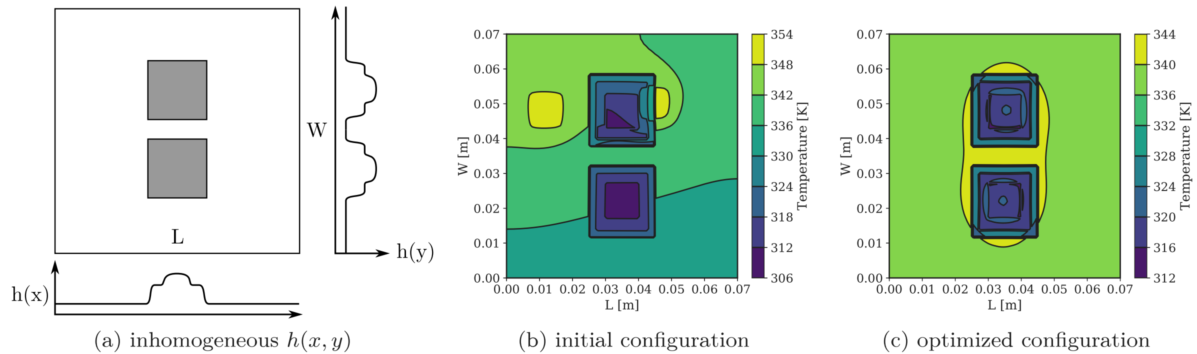

Fig. 20. Electrical component relocation in the case of two-dimensional inhomogeneous convection.

further validate this concept, the process is repeated for case B under the application of a more complex inhomogeneous distribution $h(x, y)$ which resembles the mounting of passive cooling at the other end of the substrate (Fig. 20).

The two components used for case B, whose characteristics are provided in Table 4, are relocated to occupy the two spots where the convective effect is higher (Fig. 20(c)). In both cases, each optimal thickness is the same as in Table 6. Sequential Least Square Quadratic Programming (SLSQP) is used for the optimization of both cases accounted in this Appendix.

References

[1] A. Pesaran, Battery thermal management in EVs and HEVs: Issues and solutions, in: Advanced Automotive Battery Conference, Vol. 43, 2001.

[2] K.R. Bagnall, Y.S. Muzychka, E.N. Wang, Analytical solution for temperature rise in complex multilayer structures with discrete heat sources, IEEE Trans. Compon. Packag. Manuf. Technol. 4 (5) (2014) 817–830, http://dx.doi.org/10.1109/TCPMT.2014.2299766.

[3] C. Song, J. Kim, J. Cho, The effect of GaN epilayer thickness on the near-junction thermal resistance of GaN-on-diamond devices, Int. J. Heat Mass Transfer 158 (2020) http://dx.doi.org/10.1016/j.ijheatmasstransfer.2020.119992.

[4] F. Ghioldi, J. Hélie, F. Piscaglia, A fast computational method for the optimal thermal design of anisotropic multilayer structures with discrete heat sources for electrified propulsion systems, Int. J. Heat Mass Transfer 183 (2022) http://dx.doi.org/10.1016/j.ijheatmasstransfer.2021.122114.

[5] K. Choudhury, D. Rogers, Steady-state thermal modeling of a power module: An N-layer Fourier approach, IEEE Trans. Power Electron. PP (2018) http://dx.doi.org/10.1109/TPEL.2018.2828439.

[6] B. Subedi, S.H. Kim, S.P. Jang, M.A. Kedzierski, Effect of mesh wick geometry on the maximum heat transfer rate of flat-micro heat pipes with multi-heat sources and sinks, Int. J. Heat Mass Transfer 131 (2019) 537–545, http://dx.doi.org/10.1016/j.ijheatmasstransfer.2018.11.086.

[7] T.Q. Feng, J.L. Xu, An analytical solution of thermal resistance of cubic heat spreaders for electronic cooling, Appl. Therm. Eng. 24 (2–3) (2004) 323–337, http://dx.doi.org/10.1016/j.applthermaleng.2003.07.001.

[8] S.M. Thompson, H.B. Ma, C.W. LaPierre, Thermal spreading analysis of rectangular heat spreader, J. Heat Transfer 136 (6) (2014) 1–8, http://dx.doi.org/10.1115/1.4026558.

[9] Y.S. Muzychka, J.R. Culham, M.M. Yovanovich, Thermal spreading resistance of eccentric heat sources on rectangular flux channels, J. Electron. Packag. Trans. ASME 125 (2 SPEC.) (2003) 178–185, http://dx.doi.org/10.1115/1.1568125.

[10] Y.S. Muzychka, K.R. Bagnall, E.N. Wang, Thermal spreading resistance and heat source temperature in compound orthotropic systems with interfacial resistance, in: 44th AIAA Thermophysics Conference, Vol. 3, No. 11, IEEE, 2013, pp. 1826–1841, http://dx.doi.org/10.1109/TCPMT.2013.2269273.

[11] B. Al-Khamaiseh, Y.S. Muzychka, S. Kocabiyik, Spreading resistance in multilayered orthotropic flux channel with temperature-dependent thermal conductivities, J. Thermophys. Heat Transfer 32 (2) (2018) 392–400, http://dx.doi.org/10.2514/1.T5337.

[12] A. Gholami, M. Bahrami, Thermal spreading resistance inside anisotropic plates with arbitrarily located hotspots, J. Thermophys. Heat Transfer 28 (4) (2014) 679–686, http://dx.doi.org/10.2514/1.T4428.

[13] D. Guan, M. Marz, J. Liang, Analytical solution of thermal spreading resistance in power electronics, IEEE Trans. Compon. Packag. Manuf. Technol. 2 (2) (2012) 278–285, http://dx.doi.org/10.1109/TCPMT.2011.2162515.

[14] M. O'Keefe, K. Bennion, A comparison of hybrid electric vehicle power electronics cooling options, in: 2007 IEEE Vehicle Power and Propulsion Conference, 2007, pp. 116–123, http://dx.doi.org/10.1109/VPPC.2007.4544110.

[15] K.R. Choudhury, D.J. Rogers, Steady-state thermal modeling of a power module: An N-layer Fourier approach, IEEE Trans. Power Electron. 34 (2) (2019) 1500–1508, http://dx.doi.org/10.1109/TPEL.2018.2828439.

[16] Y.S. Muzychka, Influence coefficient method for calculating discrete heat source temperature on finite convectively cooled substrates, IEEE Trans. Compon. Packag. Technol. 29 (3) (2006) 636–643, http://dx.doi.org/10.1109/TCAPT.2006.880477.

[17] D. Schweitzer, L. Chen, Heat spreading revisited - effective heat spreading angle, in: Annual IEEE Semiconductor Thermal Measurement and Management Symposium, Vol. 2015-April, 2015, pp. 88–94, http://dx.doi.org/10.1109/SEMI-THERM.2015.7100145.

[18] H.K. Yun, Y.K. Seo, H.R. Gwang, Evaluation of spreading thermal resistance for heat generating multi-electronic components, in: Thermomechanical Phenomena in Electronic Systems - Proceedings of the Intersociety Conference, 2006, pp. 258–264, http://dx.doi.org/10.1109/ITHERM.2006.1645351.

[19] C. Qian, R.K. Tan, W. Ye, An adaptive artificial neural network-based generative design method for layout designs, Int. J. Heat Mass Transfer 184 (2022) 122313, http://dx.doi.org/10.1016/j.ijheatmasstransfer.2021.122313.

[20] X. Chen, X. Chen, W. Zhou, J. Zhang, W. Yao, The heat source layout optimization using deep learning surrogate modeling, Struct. Multidiscip. Optim. 62 (2020) 3127–3148, http://dx.doi.org/10.1007/s00158-020-02659-4.

[21] K. Chen, J. Xing, S. Wang, M. Song, Heat source layout optimization in two-dimensional heat conduction using simulated annealing method, Int. J. Heat Mass Transfer 108 (2017) 210–219, http://dx.doi.org/10.1016/j.ijheatmasstransfer.2016.12.007.

[22] D.W. Hengeveld, J.E. Braun, E.A. Groll, A.D. Williams, Optimal placement of electronic components to minimize heat flux nonuniformities, J. Spacecr. Rockets 48 (4) (2011) 556–563, http://dx.doi.org/10.2514/1.47507.

[23] J.D. Mathias, P.-M. Geffroy, J.-F. Silvain, Architectural optimization for microelectronic packaging, Appl. Therm. Eng. 29 (11) (2009) 2391–2395, http://dx.doi.org/10.1016/j.applthermaleng.2008.12.037.

[24] G. Maranzana, I. Perry, D. Maillet, S. Raël, Design optimization of a spreader heat sink for power electronics, Int. J. Therm. Sci. 43 (1) (2004) 21–29, http://dx.doi.org/10.1016/S1290-0729(03)00107-8.

[25] Y.S. Chen, K.H. Chien, Y.S. Tseng, Y.K. Chan, Determination of optimized rectangular spreader thickness for lower thermal spreading resistance, J. Electron. Packag. Trans. ASME 131 (2009) http://dx.doi.org/10.1115/1.3068299.

[26] M. Razavi, Y.S. Muzychka, S. Kocabiyik, Thermal resistance in a rectangular flux channel with nonuniform heat convection in the sink plane, J. Heat Transfer 137 (11) (2015) 1–9, http://dx.doi.org/10.1115/1.4030885.

[27] The OpenFOAM Foundation, [link], URL https://openfoam.org/version/dev/.

[28] R. Fletcher, I. Bomze, V. Demyanov, T. Terlaky, The Sequential Quadratic Programming Method, 2010, pp. 165–214, http://dx.doi.org/10.1007/978-3-642-11339-0_3.

[29] S. Luhar, D. Sarkar, A. Jain, Steady state and transient analytical modeling of non-uniform convective cooling of a microprocessor chip due to jet impingement, Int. J. Heat Mass Transfer 110 (2017) 768–777, http://dx.doi.org/10.1016/j.ijheatmasstransfer.2017.03.064.

[30] S.W. Churchill, M. Bernstein, A correlating equation for forced convection from gases and liquids to a circular cylinder in crossflow, J. Heat Transfer 99 (2) (1977) 300–306, http://dx.doi.org/10.1115/1.3450685.

[31] A. Žukauskas, R. Ulinskas, Efficiency parameters for heat transfer in tube banks, Heat Transf. Eng. 6 (1) (1985) 19–25, http://dx.doi.org/10.1080/01457638508939614.

[32] J. Nocedal, S.J. Wright, Numerical Optimization, second ed., Springer, New York, NY, USA, 2006.

[33] W.A. Khan, Modeling of Fluid Flow and Heat Transfer for Optimization of Pin-Fin Heat Sinks, University of Waterloo, 2004, URL http://hdl.handle.net/10012/947.

[34] F. Gerber, R. Furrer, optimParallel: An R package providing a parallel version of the L-BFGS-B optimization method, R J. 11 (1) (2019) 352–358, http://dx.doi.org/10.32614/RJ-2019-030.